EXPERIMENTAL AND NUMERICAL STUDY ON MICROBUBBLE COALESCENCE DYNAMICS

A Thesis

Submitted to the Faculty

of

Purdue University

by

Shuyi Zhou

In Partial Fulfillment of the

Requirements for the Degree

of

Master of Science in Mechanical Engineering

December 2017

Purdue University

Indianapolis, Indiana

THE PURDUE UNIVERSITY GRADUATE SCHOOL
STATEMENT OF COMMITTE APPROVAL

Dr. Likun Zhu, Chair

Department of Mechanical Engineering

Dr. Mangilal Agarwal

Department of Mechanical Engineering

Dr. Whitney (Huidan) Yu

Department of Mechanical Engineering

Approved by:

Dr. Jie Chen

Head of the Graduate Program

For *my dear families,*
my parents and my best friends

ACKNOWLEDGMENTS

This work was sponsored by U.S. National Science Foundation under Grant No. 1335850. We would like to acknowledge the director of Integrated Nanosystems Development Institute (INDI) at IUPUI, Dr. Mangilal Agarwal for using their shared facilities (digital cutter, FESEM, etc.), and Dr. Rongrong Chen, Dr. JongEun Ryu in support of our research. I may first express my sincere gratitude to my academic advisor Dr. Likun Zhu for his continuous support, academic advice and encouragement during my research project. His kind guidance helps me all the way from using the fabrication machine, test device to conducting simulations and writing this theis. Meanwhile I would like to show many thanks to Yuanzhi Cao, and Chuanyi Chen, previous graduate and undergraduate student in Dr. Zhu's lab and in the same research project with me, and they left very practical lab materials for my further focus and use.

I would also like to show my appreciation to Dr. Whitney (Huidan) Yu, her PhD student Rou Chen and visiting scholar Senyou An, shared their GPU workstation with me to use and gave enlightening discussions. Besides, my sincerely acknowledgements go to my lab mates Dr. Cheolwoong Lim, Anna (Huixiao) Kang Tianyi Li, Xinwei Zhou for the great time we had together in the lab and their upholding for my project, especially Tianyi, run the AVIZO program, calculating pixels for my oscillation analysis. I appreciate Mr. David Briel for helping me with software and computer issues. Also I feel grateful for Mr. Jerry Mooney's assistance in my thesis format check.

Special acknowledgements to my thesis committee members Dr. Likun Zhu, Dr. Whitney (Huidan) Yu and Dr. Mangile Agwarl for their time and participation in my thesis defense. Without their kind advice and comments, my thesis work could not go easily and smoothly.

Last but not least, I give many thanks to my families, my parents Xin Zhao, and Jianbo Zhou, engineers themselves, they have always encouraged me towards excellence. My aunt and uncle Hong Stanton, Pierre Stanton, also my cousin Erika Stanton, for their love and support during my days in U.S.

TABLE OF CONTENTS

Page

LIST OF TABLES

LIST OF FIGURES

SYMBOLS

m	mass
v	velocity
μ	dynamic (shear) viscosity
ρ	density, volumetric mass density
τ	coalescence timescale
σ	surface tension coefficient
θ	capillary wave propagation angle
g	acceleration due to gravity
r_S	radius of the smaller parent bubble
r_L	radius of the larger parent bubble
r_M	radius of the new merged bubble
r	neck growth
τ_w	wall shear stress

NOMENCLATURE

H_2O_2	hydrogen peroxide solution
PS	polystyrene
P_t	platinum
O_2	oxygen in gas state at standard temperature and pressure
H_2O	water in liquid state at standard temperature and pressure
r_m	radius of merged bubble
r_S	radius of the smaller bubble before merging
r_L	radius of the larger bubble before merging

ABSTRACT

Zhou, Shuyi. M.S.M.E., Purdue University, December 2017. Experimental and Numerical Study on Microbubble Coalescence Dynamics. Major Professor: Likun Zhu.

This thesis work aims to make a better knowledge on the insights of physics on microbubble coalescence process, using experimental and numerical approaches. The neck growth and bubble surface wave propagation at the early stage of coalescence, merging preference, as well as a reaction-channel modified microfluidic gas generator are presented in the thesis.

Coalescence of unequal-sized microbubbles captive on solid substrate was observed from cross-section view using synchrotron high speed imaging technique and a microfluidic gas generation device. The bridging neck growth and surface wave propagation at the early stage of coalescence were investigated by experimental and numerical methods. The results show that theoretical half power law of neck growth rate is still valid when viscous effect is neglected. However, the inertial-capillary time scale is based on the radius of smaller parent microbubble. The surface wave propagation rate is proportional to the inertial-capillary time scale, which is based on the radius of larger parent microbubble of a coalescence pair.

Meanwhile, the relationship of preference distance and size inequality microbubbles were studied using the same micrfluidic gas generator and observation facilities. The size inequality of parent microbubbles would affect the preference distance of merged bubble in between. The merged bubble gets less closer to the larger parent bubble with an exponent of 1.82 as a reference, which largely affected by shear stress begotten on the solid interface. To express this phenomenon distinguished with free merging bubble pair, we propose the wall shear stress hinders the process of that

parent bubbles move towards to each other during coalescence Our hypothesis was confirmed by identical coalescence simulation via ANSYS Fluent.

To address the multiple measurement, utilization of Java based photography processing software ImageJ was applied as a key point to the thesis work. To acquire more microbubble coalescence cases on experiment for study, we enhanced the performance of microfluidic gas generator with reaction channel optimization. An optimized design on increasing the number of parallel reaction channel from single to triple, was applied to obtain a higher gas generation rate. Also the gas vent shape was modified from triangle to rectangle to provide more information on reaction channel optimization. The gas generation rate and H_2O_2 conversion rate were provided to further discuss.

1. INTRODUCTION

1.1 Background of Research

1.1.1 Microbubble Coalescence Process

Microbubble commonly defined as a bubble of radius range from a few micrometers to one thousand micrometers, has promising and widespread applications in biological, chemical, material and medical areas, such as active substance or surfactant for water disparate treatment process, ultrasound agents targeted for drug delivery or other material tracking, used for other therapeutic applications as carriers of gas, genes, and oxygen, in the process of sonoporation, tumor ablation, and sonothrombolysis. [1] Numerous composition of shell and filling items enable researchers to find better utilization of microbubble properties, such as buoyancy, crush strength, thermal conductivity, and acoustics.

Coalescence, or merging, one of attracting microbubble dynamics phenomenon, has drawn scientific interests since nearly century, but yet still confined by observation device, gas bubble generator, and etc. Scientists do not have a comprehensive understanding of the insight physics. [2] The coalescence process - the tendency for two touching spheres to form a single larger one - occurs as a result of the surface energy minimization and is supposed to come about at various conditions and have broad applications. The research on coalescence diversely spread with the bubble doublet size, inequality, filling gas, liquid solution as well as sessile or free on solid interface. Nowadays, most coalescence observation and analysis experimentally or numerically focus on equal-sized microbubbles unattached with any interface that is to say, free in liquid solution through effective and economic imaging processing application and high-power computational software tools. That enables researchers

to obtain very details of the merging, oscillation dynamics of a specific point on the bubble sphere during merged bubble formation and other kinematic analysis from post process. However, the effect of microbubble sessile on the solid substrate, was ignored.

Our study focused on the preference distance, motion tendency of contact point, neck growth, capillary waves propagation in the initial stage of unequal-sized of microbubble coalescence on the solid substrate.

1.1.2 Microbubble Gas Generator System

As we known, there are compressed gas, liquid hydrogen, physical adsorption on metal organic frameworks [3] and metal or chemical hydrides. But unfortunately, most of these gas storage methods are impractical for small portable power source applications such as micro fuel cell due to low energy density, complicated control units, relatively expensive cost, and the strict storage conditions. [4]

The well developed advanced microfabrication method only used patterned polystyrene (PS) films. The patterned PS films were obtained from a digital cutter and they were bonded into a microfluidic device by thermo-press bonding method that required no heterogeneous bonding agents. This new method did not need manual assembly which greatly improved its precision (100 μm), and it used only PS as device material that has favorable surface wetting property for microfluidics applications. [5]

1.2 Objectives of Research

The objectives of this research are:

1. To understand the early stage coalescence phenomena, like bridging neck growth and surface wave propagation of microbubble entrapped in the channel based on reaction experiment of microfluidic gas generator through image processing.

2. To gain the insight of coalescence preference of size inequality microbubbles and provide convinced expression.

3. To obtain proper performance of microfluidic gas generator by optimizing reaction-channel design.

1.3 Structure of Thesis

The thesis consists of 6 chapters as detailed following. Chapter 1 introduces of the research background, the objectives and the structure of the thesis.

Chapter 2 states the studies on bridging neck growth and surface wave propagation in the early stage of microbubble coalescence through experimental and numerical approaches. Corresponding power law relationship were provided.

Chapter 3 presents the coalescence preference on various size ratio of merging microbubble pairs and displacement of contact point are discussed in detail based on reaction inside the channel of microfluidic gas generation. A wall shear stress contour analysis by using ANSYS FLUENT give a potential explanation on coalescence preference.

Chapter 4 illustrates, the design of optimized parallel reaction-channel design, fabrication and experimental conduction of the microfluidic gas generator system, including the gas generating rate comparison between single channel based device and multi-channel based one.

Chapter 5 summarizes the major findings and contributions in the thesis work. Corresponding possible future work is also concisely discussed.

2. STUDY ON NECK GROWTH AND SURFACE WAVE PROPAGATION ANGLE OF MICROBUBBLE COALESCENCE

2.1 Introduction

Coalescence of microbubbles are encountered in many industrial applications when gas microbubbles are generated from or injected into liquid reactants, such as solar water splitting systems, [6–8]microbial electrolysis cells, [9–11] and gas-liquid synthesis. [12–14] Fundamental understanding of coalescence dynamics of microbubbles is essential to the design of those systems and devices. To this end, most studies on microbubble coalescence have been focused on equal-sized parent bubbles with complete spherical shape. [15] For instance, the dynamics of thinning and rupture of the liquid film between two approaching bubbles just prior to coalescence has been studied extensively. [16–19] The dynamics of bridging neck growth has been the focus of many studies. [15, 20, 21] It has been shown that the bridging neck radius r of two parent bubbles follows a power-law, $r/R \propto (t/\tau)^{1/2}$, in the early-stage of coalescence, where R is the initial radius of parent bubbles andτ is a time scale. When viscous effect is negligible, the time scale is inertial-capillary time scale $\tau = (\rho R^3/\sigma)^{1/2}$. [15] Stover et al. investigated the effects of bubble size, electrolyte viscosity, and surface tension on oscillation dynamics of coalesced bubble. [2] However, in real applications, coalescence could happen when microbubbles are captive on solid substrate with certain contact angle. In addition, the bubble sizes are different for most of the coalescence cases. Recently, Weon et al. have reported that the location of the coalesced bubble is linked by the parent bubble size ratio with a power-law relationship. [22, 23] Chen et al. reported that the coalescence time also exhibits a power-law scaling with the parent bubble size ratio. [1] However, the dynamics in the early-stage of coalescence

of two unequal-sized microbubbles captive on a solid substrate is still unknown. The objective of this paper is to investigate whether there is a universal time scaling law in such coalescence cases. In this study, coalescence of two unequal-sized microbubbles captive on a solid substrate was investigated experimentally and numerically. A special polymer microfluidic device was designed and fabricated to generate microbubbles and bubble coalescence events. An ultrafast synchrotron X-ray imaging facility at 32-ID-B in the Advanced Photon Source of the Argonne National Laboratory was used to visualize individual coalescence events inside the polymer microfluidic channel. Besides, the benefits of numerical methods allow us conduct either two dimensional or three dimensional simulation without barriers of location and timescale. Academic ANSYS FLUENT 16.0 and 18.0 packages (ANSYS, Inc. Canonsburg, PA 15317, USA) were used to simulate coalescence process for this thesis work. The bridging neck growth and surface wave propagation in the early stage of bubble coalescence were analyzed based on the imaging results and simulation results.

2.2 Experimental

Experiment and Image Acquisition

The coalescence experiment was based on microbubbles generated inside a polymer microfluidic gas generation device. The device was fabricated by aligning and sequentially stacking/thermopress bonding multiple layers of patterned polystyrene (PS) film (Goodfellow, Coraopolis, PA) which were achieved by a craft cutter (FC2250-60 VC, Graphtec, Santa Ana, CA). [5] A picture of the device and the schematic of a cross-section view of the device are shown in Figure 2.2(b). A reaction microchannel was formed by bonding a platinum (Pt) black catalyst layer inside the microchannel. The Pt black was electroplated on a gold foil (10 μm thick) with 0.1 A/cm^2 current density for 55s. The Pt density was measured and calculated to be 1.5 mg/cm^2. The gold foil was attached on a double-sided tape when being electroplated with Pt.

Then it can be attached to PS film with the other adhesive surface on the reaction channel location, as is shown in the pink part in Figure 2.1.

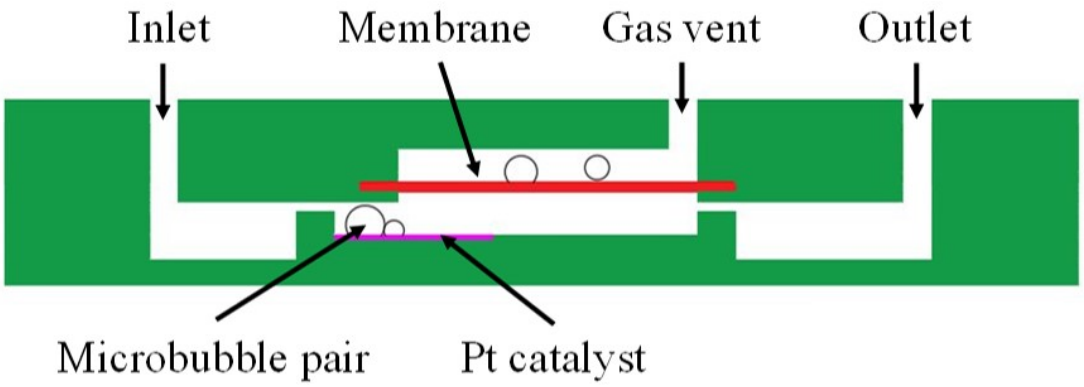

Fig. 2.1. Schematic of the cross-section view of the device.

In order to vent the gas bubble in the reaction channel, a hydrophobic nanoporous membrane (0.2 μm pore size, Sterlitech Corporation, Kent, WA) was assembled and embedded into the device, as is shown in the pink part in Figure 2.2 (b).

High-speed X-ray imaging experiments were performed at the 32-ID-B beamline of APS to visualize individual coalescence events in the reaction channel. The experimental setup is illustrated in Figure 2.2(a). An intense undulator white-beam goes through the reaction channel of the device and generates phase-contrast images of the sample. A LuAG:Ce scintillator (100 μm thickness), positioned downstream, absorbs the X-ray photons and emits visible light, which is then recorded by a high-speed camera (FastCam SA1.1, Photron), as is shown in Figure 2.2(a). It should be noted that coalescence event was visualized from the cross-section view in this study. Since the parent microbubbles are captive on the Pt catalyst substrate with 36$\circ$ contact angle, the top view cannot reveal the detailed dynamic information of bubble coalescence. To reduce the X-ray absorption in order to gain better image contrast, the longitudinal dimension of reaction channel should be as small as possible, as shown in Figure 2.2(b).

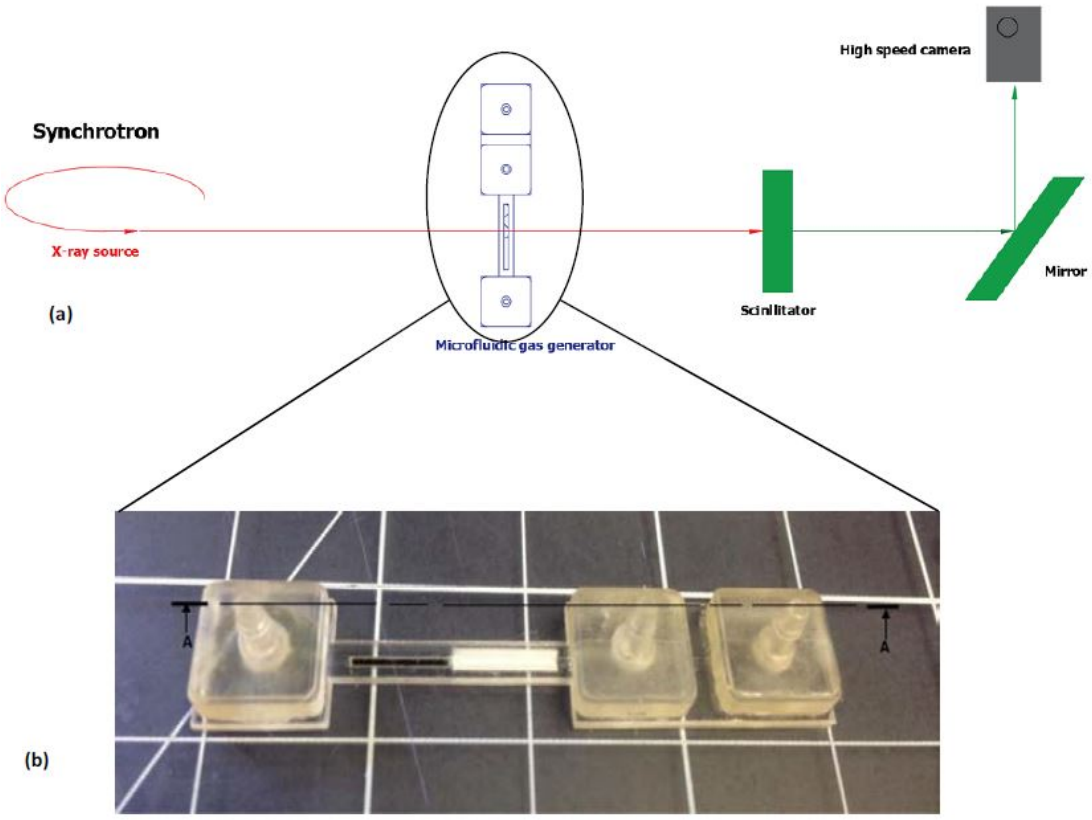

Fig. 2.2. (a) Schematic view of X-ray synchrontron imaging facility and (b) a picture of the fabricated polymer microfluidic gas generation device.

In this study, the reaction channel width is 0.7 mm with 1.15 mm PS wall on each side. 30% hydrogen peroxide (H_2O_2) was used as reactant solution in this experiment. The catalytic reaction is triggered by contacting the Pt catalyst and H_2O_2 produces water and oxygen gas. To avoid the influence of X-ray on H_2O_2, we optimized the X-ray dose to make sure H_2O_2 did not have obvious self-reaction under existence of the X-ray while the contrast of the image remained decent. As shown in Figure 2.3, the phase-contrast X-ray image clearly shows the profiles of microbubbles and other substances with 2 μm spatial resolution.

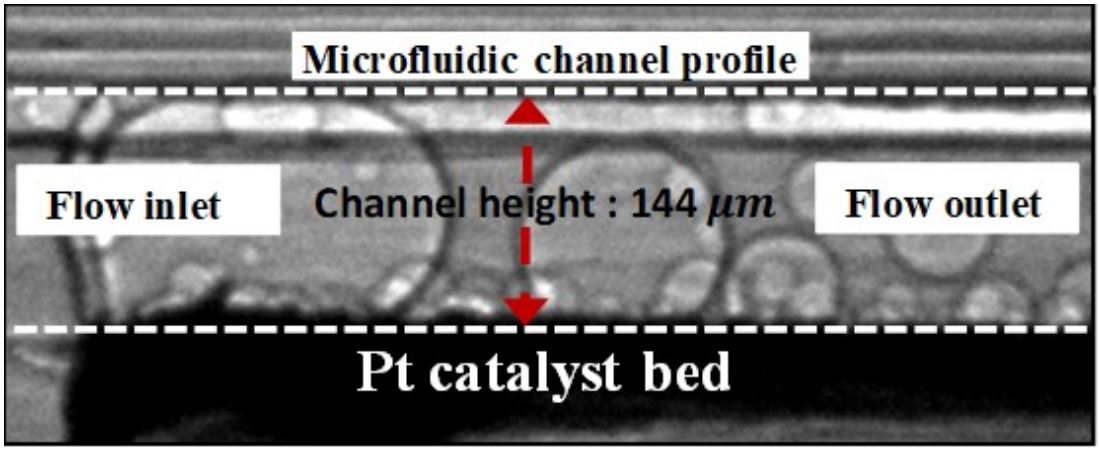

Fig. 2.3. Phase contrast image of a microbubble pair.

ANSYS FLUENT Simulation

ANSYS FLUENT CFD Development

ANSYS FLUENT one of the important computational part of ANSYS software, is widely used in many commercial and academic fluidic areas. The capability of varies physical models, precise mesh modification, and boundary condition classification, finite element calculation, as well as broad categories of post processing, enable users to simulate numerous fluidic scenarios. For instance, piping flow, turbulence, vent cooling, fuel combustion and reactions for industrial applications. A phenomenon like multiphase flow is ordinary in many industrial or research processes, amongst them the petroleum, gas industry and microbubble coalescence study. It's challenging to acquire a consistent software for multiphase analysis and simulation, based on its complexity. It's just a while for computational fluid dynamics (CFD) being a reliable tool for multiphase flow analysis, since it solved the field of single phase flow analysis for more than 20 years. The key point of obtaining the competence of applying CFD in an insightful way, is to make investigation, comprehension and validation in many models using provided commercial codes of multiphase models.

Meanwhile ANSYS mesh allow users to an automated high-performance mesh of all parts in a model for different solutions with several single mouse clicks. Additionally, full controls over the options used to generate the mesh are available for the expert users who wants to fine-tune it. It indeed utilizes the advantages of Finite Elements processing to manipulate large calculation work of matrix to produce accurate, efficient analysis study. There is no specific case study on unequal-sized of microbubble pairs merging affected at the solid interface using ANSYS FLUENT or related software and no parallel comparison on how mesh shape, number of elements influence the coalescence and corresponding mesh optimization. [24]

Volume Fraction Equation and Explicit Approach

In order to accurately resolute the microbubble coalescence, the theory behind the CFD (Computational Fluid Dynamics) finite element formulation was well understood. Using ANSYS FLUENT, theoretical equations are applied for different mode of fluids and phases, even conditions. [24]

For our case, we have two phases of viscous fluid, one liquid H_2O_2 flow and another is O_2 gas bubbles. Owing that phases dont interpenetrates each other, we select the model setting as Volume of Fluid (VOF) in ANSYS FLUENT. The tracking of the interface(s) between the phases is accomplished by the solution of a continuity equation for the volume fraction of one (or more) of the phases. [25] For the q^{th} phase, this equation has the following form:

$$\frac{1}{\rho_q}[\frac{\partial}{\partial t}(\alpha_q \rho_q) + \nabla \cdot (\alpha_q \rho_q \bar{v_q}) = S_{\alpha_q} + \sum_{p=1}^{n}(\dot{m}_{pq} - \dot{m}_{qp})]$$

where $\dot{m}_{qp}$ is the mass transfer from q phase to p phase and $\dot{m}_{pq}$ is the mass transfer from p phase to q phase. Normally ANSYS FLUENT default $S_{\alpha_q} = 0$ or constant defined by user. [24,25] the q^{th} fluids volume fraction in the cell is denoted as α_q, then the following three conditions are possible:

- α_q=0: The cell is empty (of the q^{th} fluid).

- α_q=1: The cell is full (of the q^{th} fluid).
- $0 < \alpha_q < 1$: The cell contains interface between q^{th} fluid and one or more other fluid.

The above equation be solved for the primary phase; the primary-phase volume fraction will be computed based on the following constraint $\sum_{p=1}^{n} \alpha_q = 1$. The volume fraction equation will be solved through explicit time discretization based on microbubble coalescence environment. In this case, primary phase is O_2 and secondary phase is H_2O_2. [26]

In the explicit approach, ANSYS FLUENT standard finite-difference interpolation schemes are applied to the volume fraction values that were computed at the previous time step.

$$\frac{\alpha_q^{n+1}\rho_q^{n+1} - \alpha_q^n \rho_q^n}{\Delta t} V + \sum_f (\rho_q U_f^n \alpha_q^n, f) = [\sum_{p=1}^{n} (\dot{m}_{pq} - \dot{m}_{qp}) + S_{\alpha_q}]V$$

Where,

n+1=index for new (current) time step

n=index for previous time step

α_q^n, f face value of the q^{th} volume fraction, computed from the first- or second-order upwind, QUICK, modified HRIC, compressive, CICSAM scheme.

V=volume of cell

U_f Volume flux through the face, based on normal velocity.

When the explicit scheme is used, a time-dependent solution must be computed. The solver for this case is transient. The explicit scheme and the implicit scheme treat these cells with the same interpolation as the cells that are completely filled with one phase or the other (that is, using the standard upwind (First-Order Upwind Scheme), second-order (Second-Order Upwind Scheme), QUICK (QUICK Scheme), modified HRIC (Modified HRIC Scheme), compressive (The Compressive and Zonal Discretization Schemes), or CICSAM scheme, rather than applying a special treatment. [25]

Material Properties

The properties appearing in the transport equations are determined by the presence of the component phases in each control volume. [24] In a two-phase system, if the phases are represented by the subscripts 1 and 2, and if the volume fraction of the second phase is being tracked, the density in each mesh element is given by

$$\rho = \alpha_2\rho_2 + (1 - \alpha_2)\rho_1$$

In general, for a two-phase system, the volume-fraction-averaged density takes on the following form:

$$\rho = \alpha_1\rho_1 + \alpha_2\rho_2$$

Momentum Equation

A single momentum equation is solved throughout the domain phase, and the resulting velocity field is shared among all phases. The momentum equation, shown below, is dependent on the volume fractions of all phases through the properties and ρ and μ. [27]

$$\frac{\partial}{\partial t}(\rho\bar{v}) + \nabla \cdot (\rho\bar{v}\bar{v}) = -\nabla p + [\mu(\nabla\bar{v} + \nabla\bar{v}^T)] + \rho\bar{g} + \bar{F}$$

Energy Equation

The energy equation, also shared among the phases, is shown below.

$$\frac{\partial}{\partial t}(\rho E) + \nabla \cdot (\bar{v}(\rho E + \rho)) = \nabla \cdot (k_{eff}\nabla T) + S_h$$

The VOF model treats energy E, and temperature T, as mass-averaged variables:

$$E = \frac{\sum_{p=1}^{n} \alpha_q\rho_q E_q}{\sum_{p=1}^{n} \alpha_q\rho_q}$$

Where E_P for each phase is based on the specific heat of that phase and the shared temperature. The properties and k_{eff} (effective thermal conductivity) are shared by

the phases. The source term, S_h, contains contributions from radiation, as well as any other volumetric heat sources. [24]

Time Dependence

For time-dependent VOF calculations, ANSYS FLUENT automatically refines the time step for the integration of the volume fraction equation, time step calculation can be equivalently modified by Courant number.

$$C = \frac{u\Delta t}{\Delta x} \leq C_{max}$$

Δx is the minimum cell size, that is the mesh element size in u the velocity. The value of C_{max} is dependent on the method used to solve the system of algebraic equation. For Explicit approach C_{max} should be no more than 1. [28] Knowing Δx and u and limiting C_{max}, comes up with a time step. But for more accurate we used 'variable time step option', as u velocity of microbubbles may vary during merging process.

Surface Tension

Surface tension rises as a result of attractive forces between molecules in a fluid. [29] Consider gas bubble at the surface, however, the gradient force of bubble radially outward with gas, radially inward intermolecular attractive force generated by surrounding fluid inward, together with surface tension around the bubble sphere, maintaining an equilibrium state with minimax energy in such instances. [30]

In ANSYS FLUENT, two surface tension models exist: the continuum surface force (CSF) [31] and the continuum surface stress (CSS). The two models are described in detail in the sections that follow. In this case, we chose CSF and the formulas corresponding to emphasize surface tension effect on microbubble coalescence pressure change is shown below:

$$p_1 - p_2 = \sigma(\frac{1}{R_1} + \frac{1}{R_2})$$

where P_1 and P_2 are the pressures in the two fluids on either side of the interface. The continuum surface force (CSF) model proposed by Brackbill et al. [32] has been implemented such that the addition of surface tension to the VOF calculation results in a source term in the momentum equation. It can be shown that the pressure drop across the surface depends upon the surface tension coefficient, σ, and the surface curvature as measured by two radii in orthogonal directions, R_1 and R_2. [33]

Wall Adhesion

Additionally, ANSYS FLUENT supports the specification of a wall adhesion angle in conjunction with the surface tension model in the VOF model. The model is taken from work done by Brackbill et al. Rather than impose this boundary condition at the wall itself, the contact angle θ_w that the fluid is assumed to make with the wall is used to adjust the surface normal in cells near the wall. This so-called dynamic boundary condition results in the adjustment of the curvature of the surface near the wall. [34]

If θ_w is the contact angle at the wall, then the surface normal at the live cell next to the wall is

$$\hat{n} = \hat{n}cos\theta_w + \hat{t}_w sin\theta_w$$

In our study, θ_w is 36° measured from coalescence microbubbles in experiment.

Simulation and Post-processing

The basic idea of coalescence modeling in ANSYS FLUENT is to first construct a 2D or 3D geometry, more precisely in our case, channel bearing multiple fluid phases and properties. Then adaption of regions is to patch microbubble pair in the channel. The initial position of microbubble pair is lightly touching each other, no overlap or intersection.

Model Details

For general modeling, there are following steps:

1. Build up geometry; we define a 250×220 μm surface for 2D cases, and a 250×220×200 μm extruded solid body for 3D cases. The geometry and channel boundary arrangement of 2D and 3D case are separately companying as below in Figure 2.4 and 2.5:

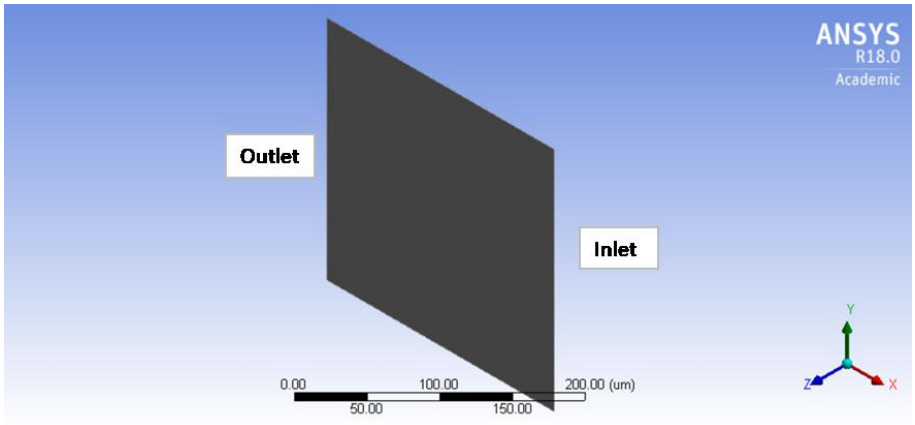

Fig. 2.4. 2D geometry model. Labels in the figure point out the inlet and outlet of channel. Microbubbles would stay at either top or bottom edge.

2. Mesh channel region and name sections; same as we learned from finite element analysis, different meshing methods will greatly affect the final results for the same problem. In these steps, we used several different mesh methods or types and we tried to find the best way by comparing those mesh. To find the effect of meshing shapes, we compare tetrahedral and cubic elements. To find the effect of meshing sizes, we compare different sizes of each edge 10 μm and 0.8 μm for 3D tetrahedral elements; 10 μm and 1 μm for hexahedron elements. Besides, we used multi-zone mesh mixer, and compare with uniform mesh in hex meshes.

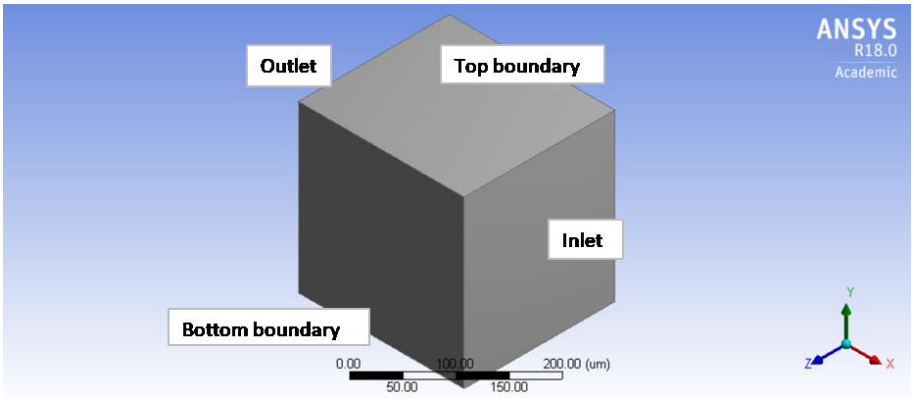

Fig. 2.5. 3D geometry model. Labels in the figure illustrate the inlet and outlet of channel, and microbubbles are sessile on either top or bottom surface.

3. Define models, materials, phases, modify boundary conditions, periodic zone setting and so on. For 2D cases, both inlet and outlet edge are periodic boundaries and same thing for enclosing surface of 3D cubic channel as microbubbles only or probably attach at the top and bottom surface during coalescence process. Density of H_2O_2 is 1060 kg/m^3 and viscosity is 1.06 $mPa{\cdot}s$, Surface tension coefficient is 0.073 N/m. Time step size is 0.1 μs dependent on Courant number variation. Density of O_2 is 1.2999 kg/m^3, and viscosity 1.919-02 $mPa \cdot s$. Make adaption of the gas bubble is to patch a bubble sphere region in the channel. The initial position is that two microbubbles are close properly to each other or in touch gently.

4. Solution method: PISO for fluids of multi-phase calculation.

5. Initialize ‘1 ‘for H_2O_2 solution and ‘0 ‘for O_2 sphere patch especially.

6. Run calculation.

7. CFD-Post results processing volume fraction in ISOSURFACE control panel to obtain image sequence for coalescence process and wall shear stress contours as well.

2.3 Results and Discussion

Meshing Comparison

Table 2.1. shows convergence test on mesh shape and size. For 3D model, ANSYS FLUENT enables hexahedron, tetrahedron or combination of both via multi-zone operation as mesh element, while corresponding to 2D model is prism, triangle and their mix (see details about the size, shape, and geometry of mesh element in Figure 2.6 and 2.7).

Table 2.1.
Convergence Test on mesh shape and size for 3D and 2D modeling

Size & shape	2D	3D
$10\mu m$ prism/hex	$\times$	$\surd$
$10\mu m$ tri/tetra	$\times$	$\surd$
$1\mu m$ prism/hex	$\surd$	$\star$
$1\mu m$ tri/tetra	$\surd$	$\star$
Multizone	$\surd$	$\star$

$\star$ denotes reasonable merging phenomena contrast to experiment.

$\surd$ denotes simulation outcome doesn't match the phenomena in experiments.

$\times$ denotes simulation can't be run.

Based on different mesh shape and size, 8 coalescence cases conducted on both 2D and 3D channel. Meshing of 2D channel is one thin slice of 3D geometry, but less elements and nodes save lots of calculation itineraries, memory, storage of program as well as timing. Mesh element of edge size 10 μm neither 2D nor 3D has a reasonable merging process (see Figure 2.8). However, 3D of hexahedron shape and mesh edge of 1 μm modeling gives much smoother appearance of microbubble, especially dealing with solid interface and time-saving. For multi-zone design, specified area with much smaller size mesh results in same phenomena but longer simulating time.

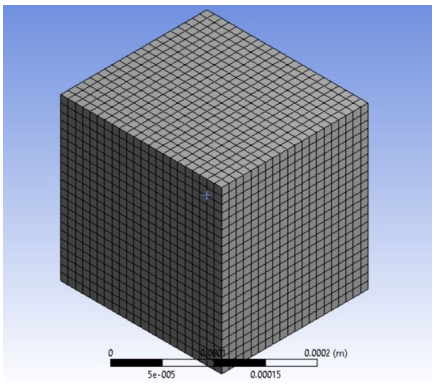

(a) 3D Hex element, size of each edge is 10 μm.

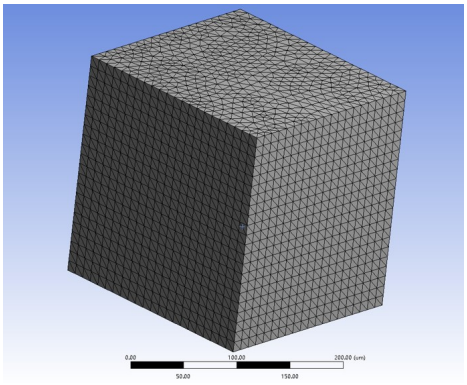

(b) 3D Tetra element, size of each edge is 10 μm.

Fig. 2.6. 3D Meshing with same edge size and different shape.

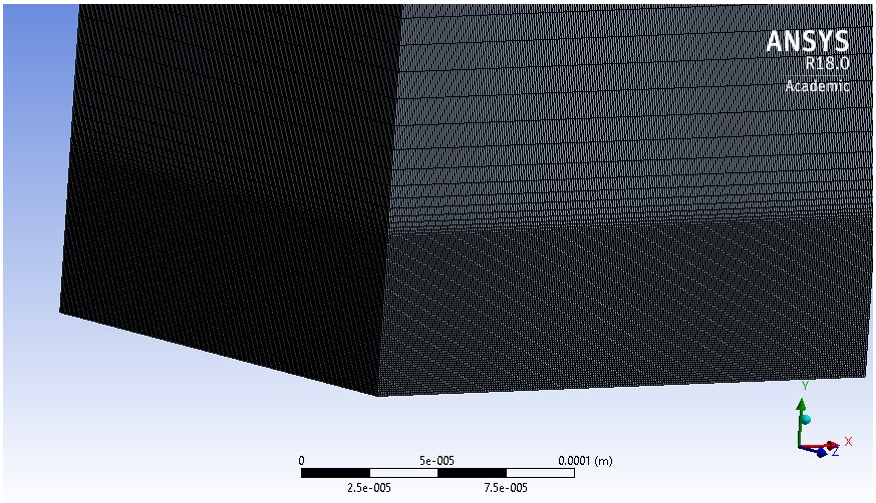

Fig. 2.7. Representative 2D unequal-sized microbubble pair merging process.

By validating the simulated coalescence process with corresponding image sequence obtained from experiment, 3D microbubble merging process (see Figure 2.10) basically tailors characteristic behaviors in same time interval. 2D modeling (shown in Figure 2.9) implies weakness of O_2 bubble periphery on changing outline near the ground gradually. The outline stagnation of 2D microbubble modeling presents more adaption considered to meet the requirements of merging process.

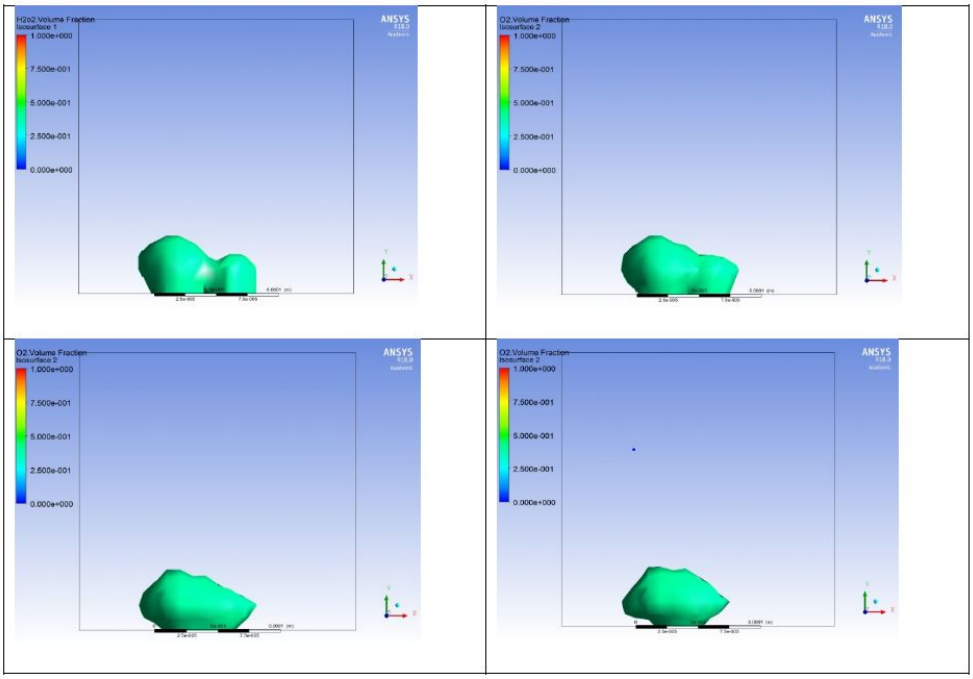

Fig. 2.8. Failed representative 3D unequal-sized microbubble pair merging process.

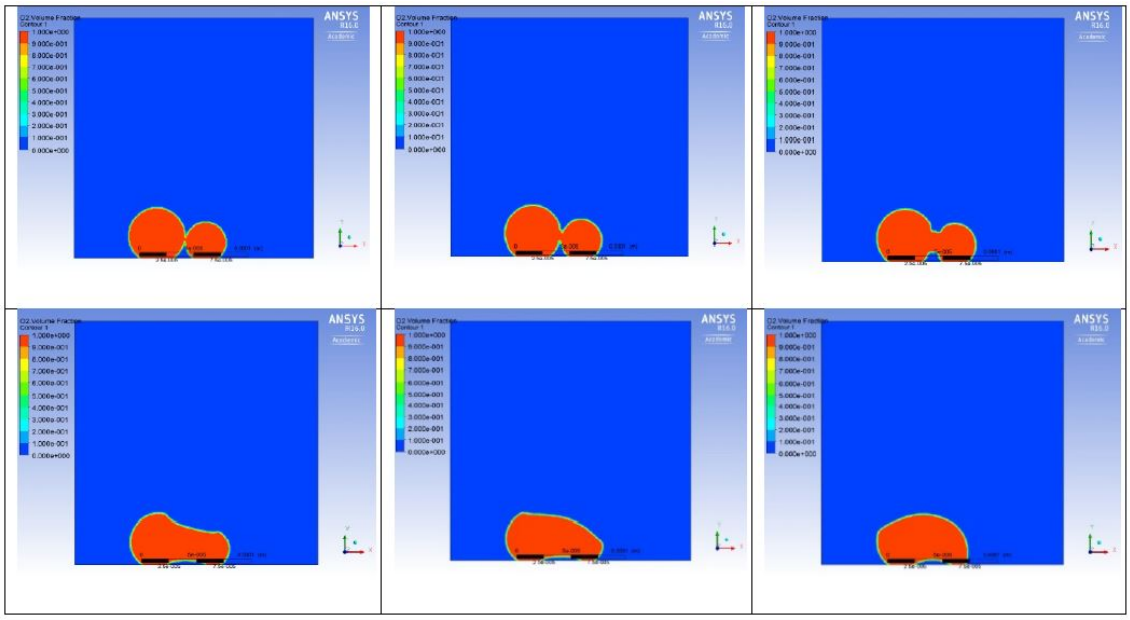

Fig. 2.9. Failed representative 2D unequal-sized microbubble pair merging process.

The pictures above illustrate the simulation of the mirobubbles connection process. Both bubbles are oxygen in H_2O_2 solution, and adhere to the wall by proper contact angle (36°). In the first picture, the two parent bubbles were about to connect to each other, and the contact boundaries between them are very clear. When the two parent bubbles form a contact between each other, the Laplace pressure difference, would cause them form together to a bigger bubble. In the second picture, we can find that the two bubbles start connecting; but at the middle of the connection, there's an 'inert point', which means two bubbles can form connection in this point. The contact boundaries disappearing take place later, as soon as the two bubbles have formed the joint meniscus, with a partial saddle in the middle. Since the bubble merging happen very fast, and with the merging of two bubbles into one bubble, the periphery of the bubbles also needed to change and rearrange accordingly, including the total surface area, volume of the bubbles and surface energy.

However, even in the last picture, where the two bubbles are already merge to each other, the 'inert point' is still there; since this 'inert point' is different from the fact, we might conclude that this simulation is good in illustrating the merging process, but fail to simulate the detail, for example, the 'inert point' should be disappear at the beginning of two bubbles merging.

In addition, tetrahedron element in latest released ANSYS FLUENT user manual is confirmed not suitable for dealing with surface tension. So we do not recommend simulation utilizing structured mesh via ANSYS FLUENT.

2.3.1 Microbubble Coalescence Modeling

Image study on ANSYS FLUENT simulation case is enabled using same photography processing software - ImageJ, and the procedures of pixel measurement is similar to what we had done with image sequence captured from experiment. The scaled channel frame shown in Figure 2.10, 2.11, 2.12, to actual dimension is 2.16^3.

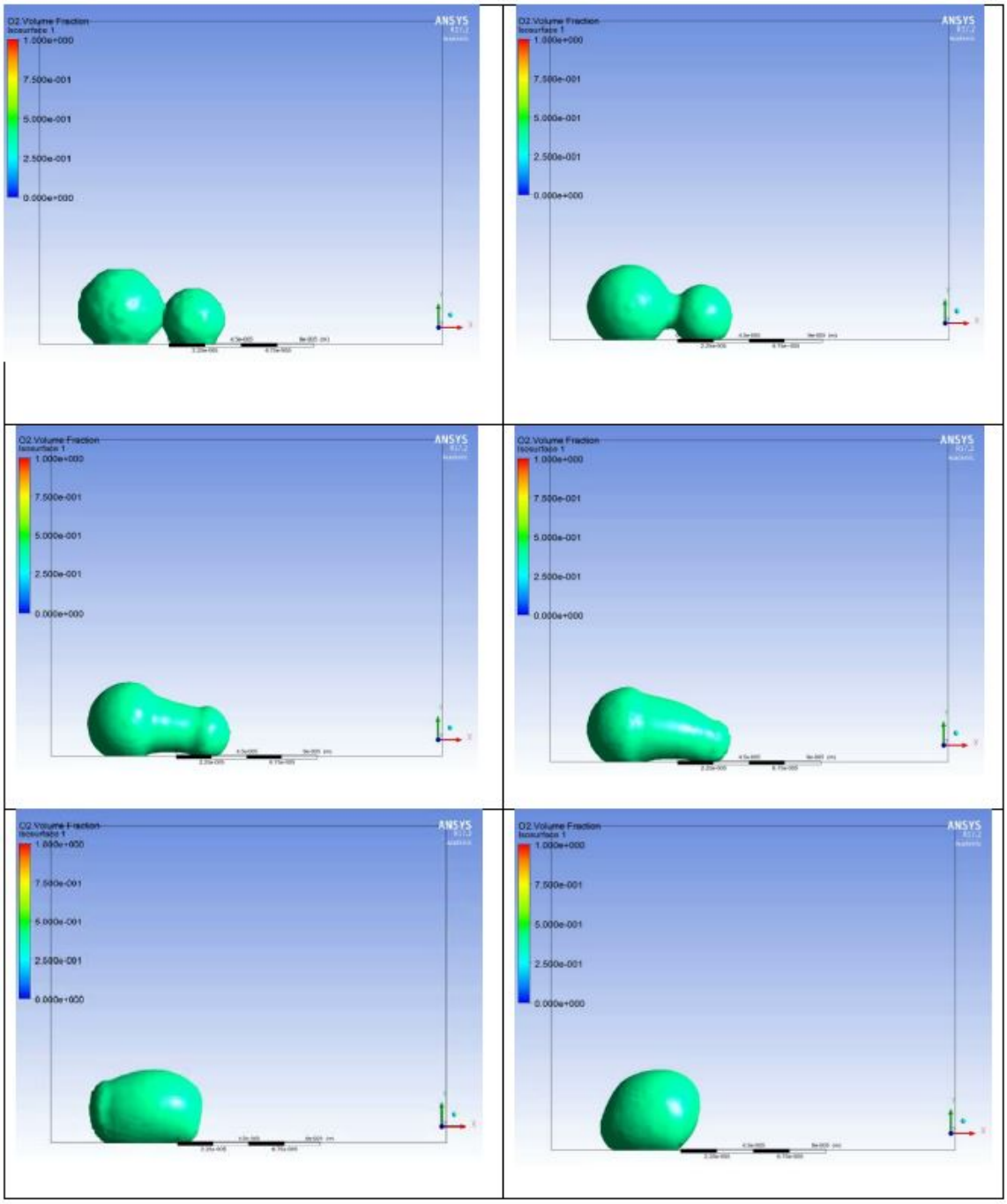

Fig. 2.10. Representative 3D unequal-sized microbubble pair merging process.

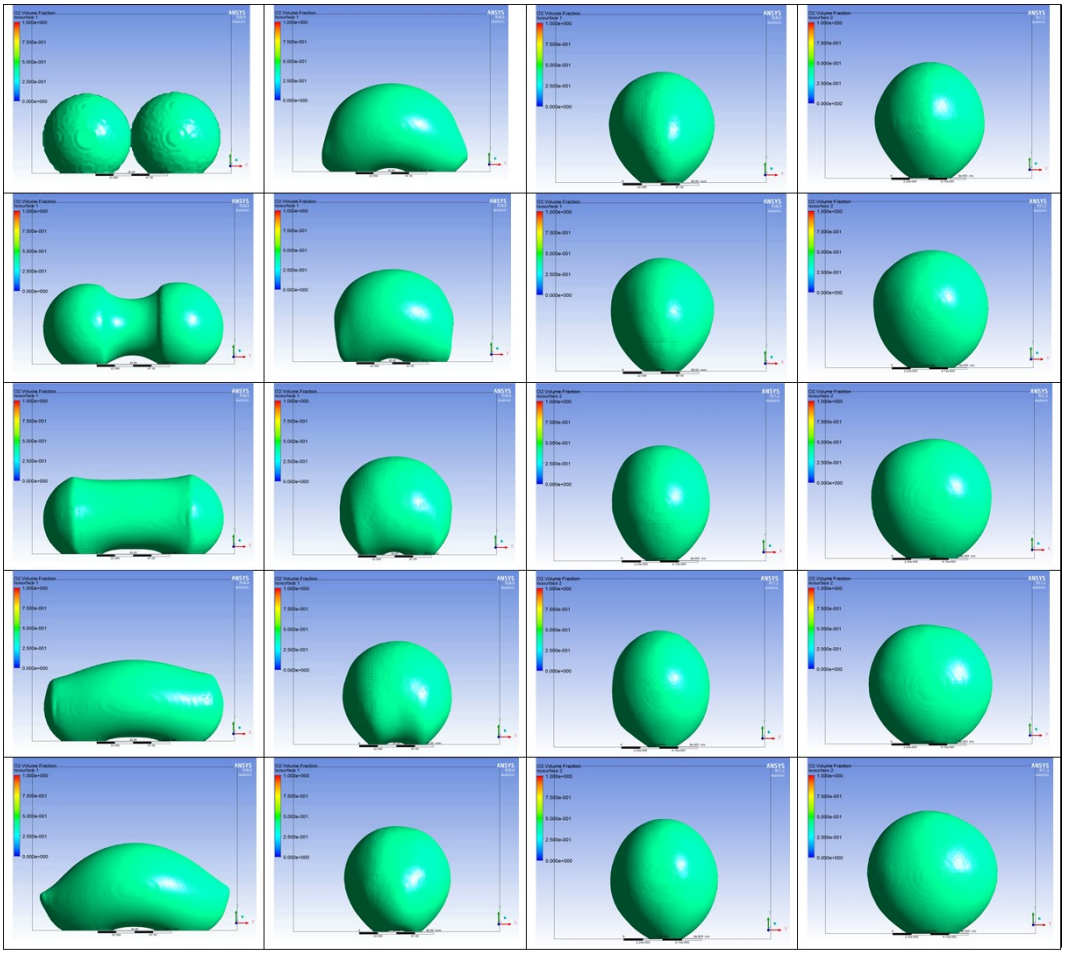

Fig. 2.11. 3D equal-sized microbubble pair merging process. The interval of each figure is 10 μs same as the one in experiment.

As the small bubble conjuncts the large bubble, the H_2O_2 in between is compressed, drained out, and circulated back to balance the volume distribution. [35] Due to the surrounding fluid, the mutual interaction as well as solid interface, the flow structure and the wall shear stress contour dramatically change from a two-independent bubble form to a single bubble form. To encounter these dynamic flow structures, the shape of the merger also has gradually changes from prolate-cusped to elongated oblate-cusped. Suppressed by surface tension, the flow structure, and

energy minimum balance, the shape of the merger changes from oblate-cusped to spherical. [36]

Owing to larger Laplace pressure from the small bubble to the large one, the coalescence process of unequal-sized has intense transformation than the one of equal-sized microbubble pair. The kinetic energy distribution transfers from small bubble to large bubble.

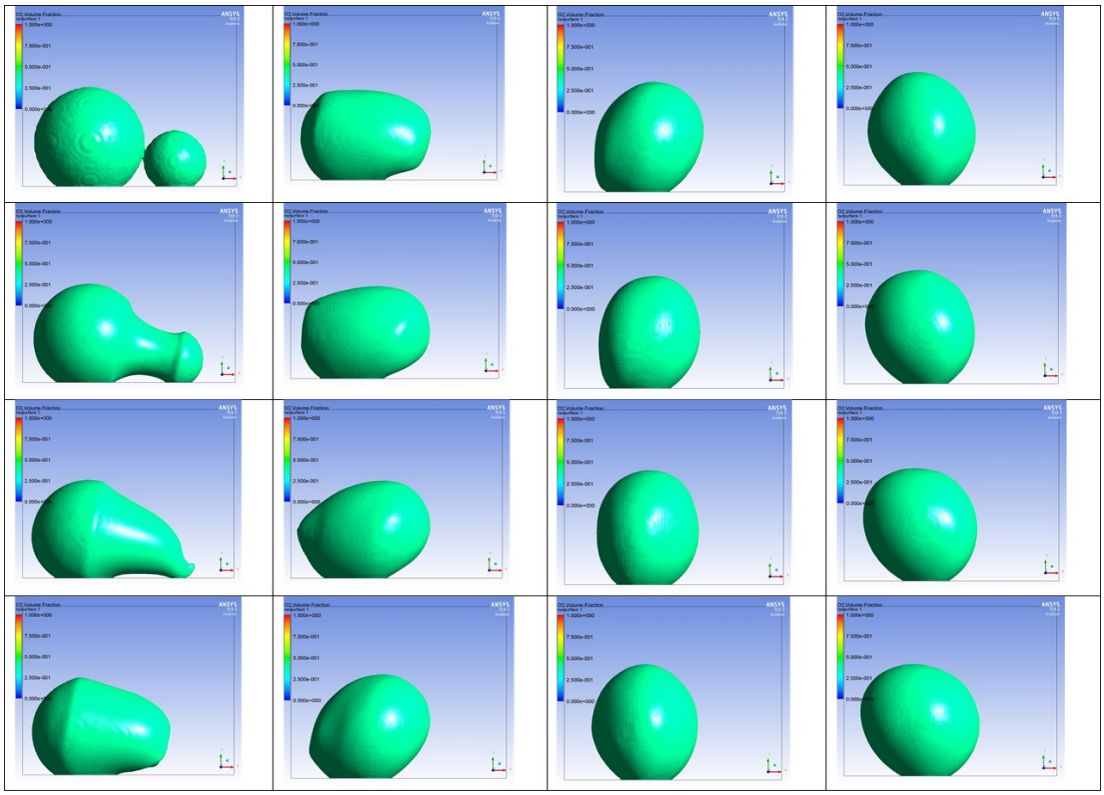

Fig. 2.12. 3D unequal-sized microbubble pair merging process. The interval of each figure is 10 μs same as the one in experiment.

2.3.2 Neck Growth and Surface Wave Propagation Study

The imaging technology allows to directly observe captive microbubble coalescence inside the reaction channel from the cross-section view. While traditional optical

technique utilized by previous experimental studies was not capable to conduct this study, due to the strong reflection or scattering effects that are usually associated with visible light imaging. In addition, the specific featured microfluidic gas generator supplies a feasible opportunity to extract cross-section view of captive bubbles on the solid substrate, due to the strong reflection or scattering effects that are usually associated with visible light imaging. [37] In addition, the specific featured microfluidic gas generator supply a feasible opportunity to extract cross-section view of dynamics captive bubbles on the solid interface.

Figure 2.13 demonstrates an example of two unequal-sized microbubbles merging into a bigger one. The whole coalescence process took place in 170 μs. A serial of images were taken by the high speed camera at a frame rate of 10^5 fps. During the imaging process, H_2O_2 solution had flow motions inside the reaction channel and oxygen generation took place continuously. It is necessary to identify whether the flow motion and oxygen generation have impact on the individual coalescence event. It can be seen from the images shown in Figure 2.13 that all other bubbles do not have clear change during the 170 μs. We can conclude that the flow motion and oxygen generation were in a relatively low speed and they do not have impact on individual coalescence event. In Figure 2.13 at 0 μs, two microbubbles with diameters 64 μm and 36 μm respectively were about to contact each other. The coalescence of the two microbubbles took place in a very short period of time and in the next frame after 10 μs, the two microbubbles have formed the bridging neck, with an arch shape in the middle. From frame 10 μs to 60 μs, we can observe that a surface wave on the interface of liquid and gas travels on the larger bubble. During this period, the shape of the coalesced microbubble showed significant dynamic change. From 70 μs to 170 μs, the coalesced bubble does not show large shape change and slowly restored the spherical shape with 36 $^\circ$ contact angle at 170 μs. During merging the equal-sized microbubbles displayed in Figure 2.14, remain the symmetrical shape transforms from that.

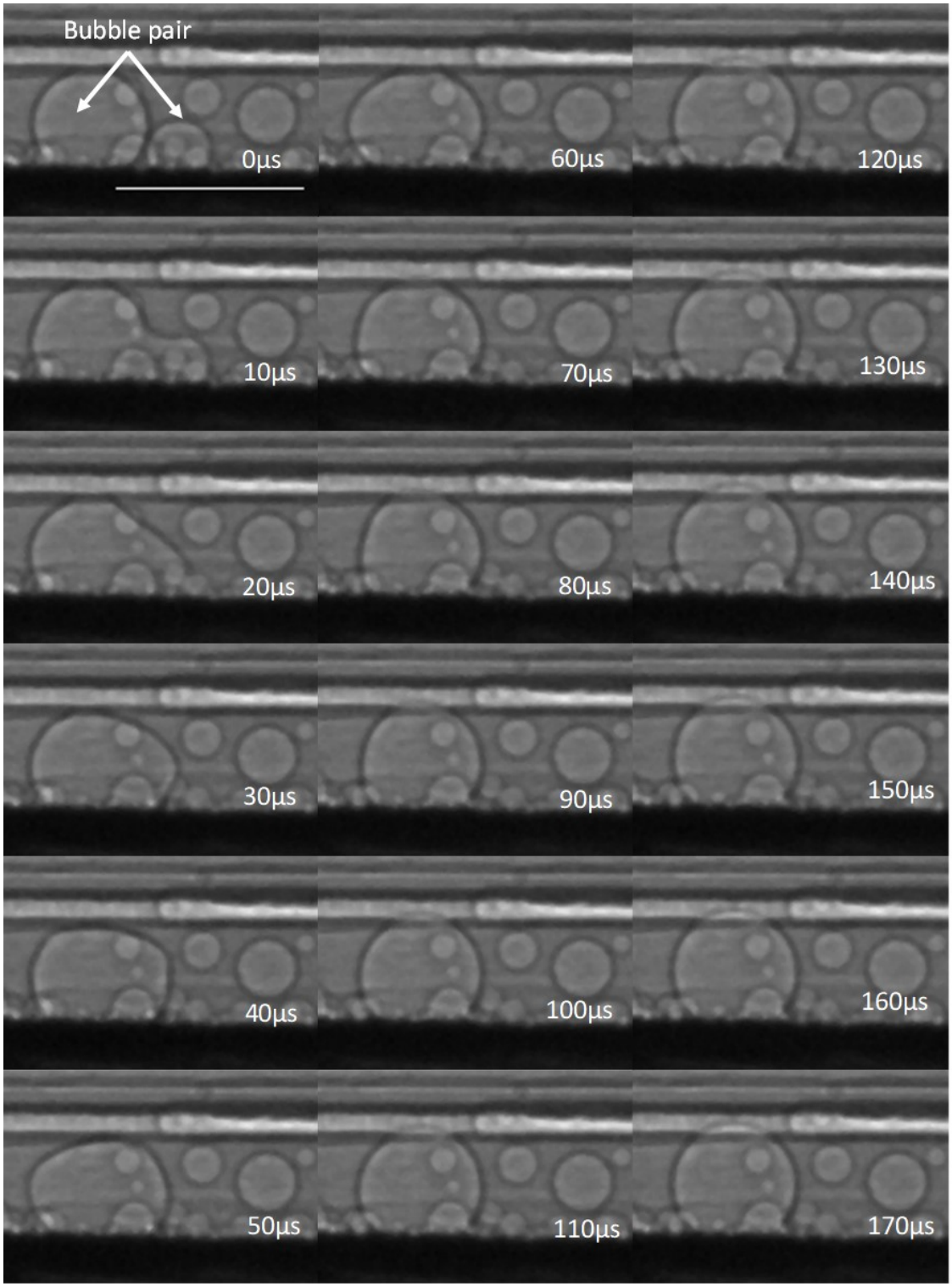

Fig. 2.13. Representative image sequence of unequal-sized bubble coalescence. This is case No. 7 mentioned in Table 3.1.The radii of two parent microbubbles in above are 64 μm and 36 μm, respectively. The whole coalescence process completed in 170 μs. The scale bar is 200 μm.

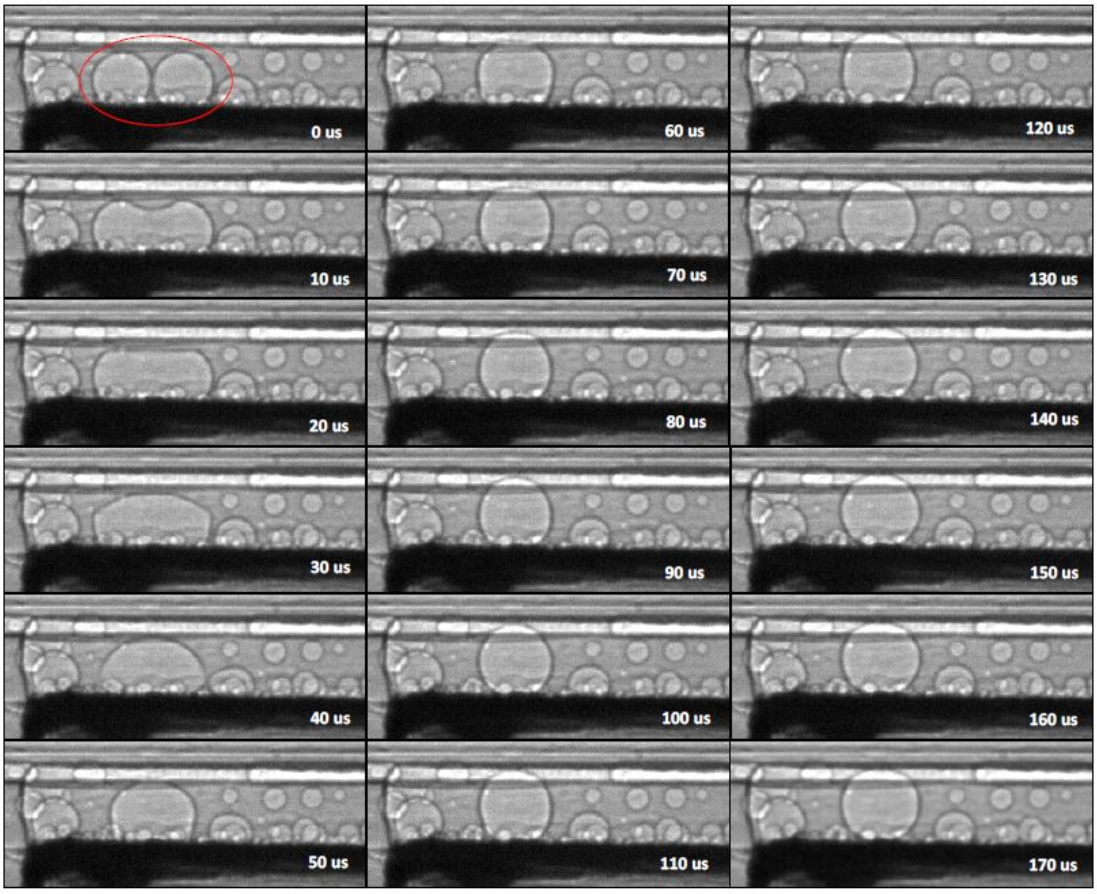

Fig. 2.14. Representative image sequence of equal-sized bubble coalescence. This is case No. 6 mentioned in Table 3.1.

The walls once separating them go flat to the condition that the boundaries of two microbubbles were inclined to a smooth pentagon, also meniscus impressed by the channel substrates, then shaped into an ellipse with tiny displacement in the vertical direction off the bottom substrate and finally become a new microbubble back to the ground, which explains that the sudden motion provided relative high kinetic energy for the microbubbles, therefore enabling a series of oscillating movement for the merged microbubble and also indicates high kinetic energy of the microbubble after the merging, and the energy was dissipated to the peripheral environment through the bouncing-like activity.

As shown in Figure 2.13, when two separate microbubbles contact each other, the formation of a bridge occurs and the bridge neck grows rapidly in the early stage of coalescence. The measurement of the neck radius for equal-sized microbubble pair is a distance from the middle point in the center line through two parent microbubbles to the saddle point of the merged surface. The determination of neck radius for unequal-sized microbubble pair is more complex than the same size pair. The neck radius is the perpendicular distance from the saddle point of the merged surface to the line through two parent microbubble centers, as is shown in Figure 2.15(a).

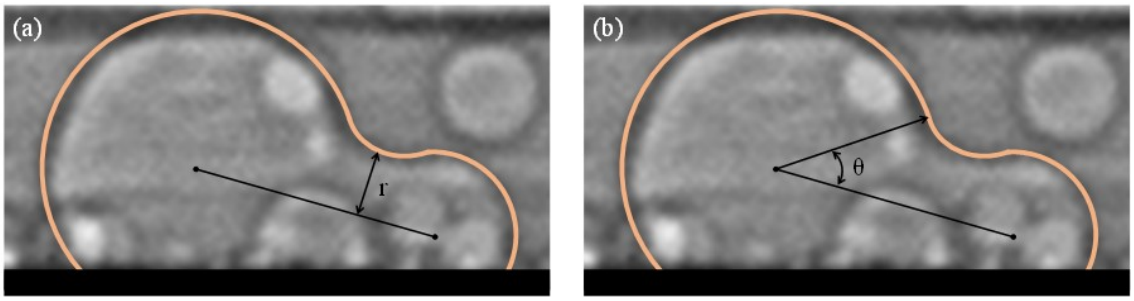

Fig. 2.15. Schematic of the measurement of (a) neck growth and (b) surface wave propagation angle during coalescence of unequal-sided microbubbles.

Previous studies have shown that the neck radius r of equal-sized bubbles follows a power-law, $r/R \propto (t/\tau)^{1/2}$, in the early stage of coalescence, where R is the initial radius of parent bubbles and $\tau = (\rho R^3/\sigma)^{1/2}$ is inertial-capillary time scale, when viscous effect is negligible. In this study, coalescence dynamics of unequal-sized microbubbles was investigated and we want to answer the following three questions. (1) Does a universal power law exist for the bridging neck growth? (2) Does the size ratio have an impact on the neck growth dynamics? (3) What is the characteristic length in the unequal-sized events were selected to perform this investigation with radius ratio 1.02 (56 μm and 55 μm), 1.45 (42 μm and 29 μm), and 1.78 (64 μm and 36 μm). It is considered that the bridging neck growth process is complete when the neck radius is the same as the radius of smaller parent microbubble. Neck growth measurement based on X-ray images was aided by an image processing and analysis program, Im-

ageJ (National Institutes of Health). If the radius of the smaller microbubble was chosen as the characteristic length, the yellow circle markers in Figure 2.15 and the dash fitting line show that the neck growth evolution follows a half power-law in the early stage of coalescence, $r/R_S \sim 1.38(t(\tau_S)^{1/2}, \tau_S = (\rho R_S^3/\sigma)^{1/2}$, with coefficient of determination R^2=0.9709. However, due to the extremely fast evolution of bridging neck, the high speed camera with 10^5 fps only can capture one or two points for those three cases. As shown in Figure 2.16, there are four points in total. In order to obtain more data points, we conducted 3D simulation in the same conditions, including microbubble and solution properties, surface tension, contact angle, size ratio etc. using ANSYS FLUENT (ANSYS, Inc. Canonsburg, PA 15317, USA). Density of H_2O_2 solution is 1060 kg/m^3 and its viscosity is 1.06 $mPas$, Surface tension coefficient is 0.073 N/m. Density of O_2 is 1.30 kgm^3 , and viscosity of O_2 is 1.92e-02 $mPa \cdot s$. Time step size is set as 0.1 μs. The initial position is that two microbubbles are in touch.

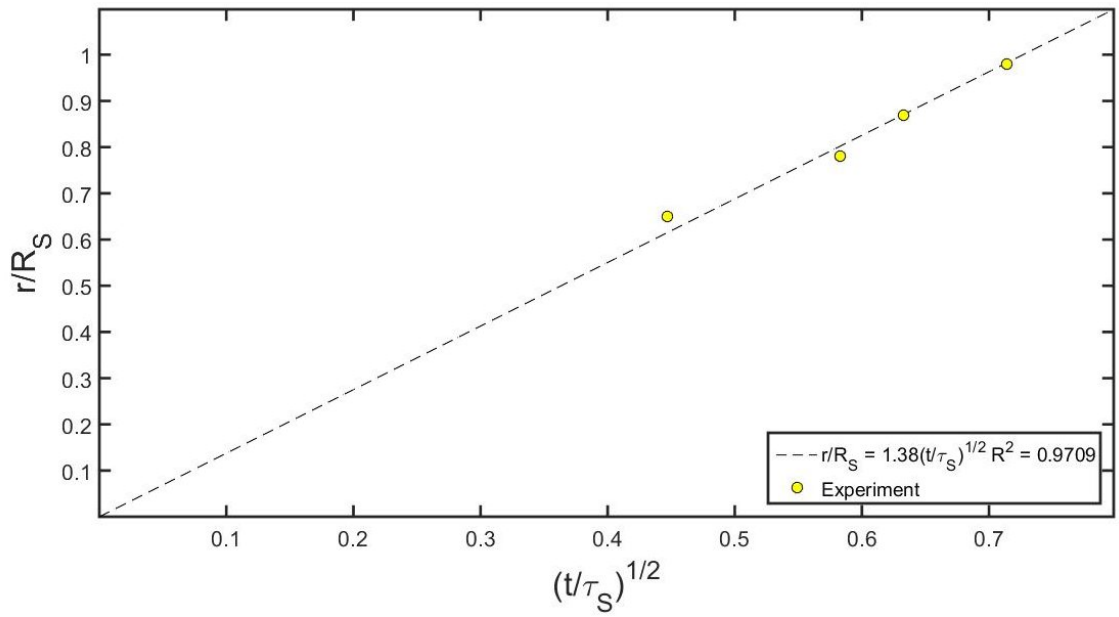

Fig. 2.16. Time evolution of neck growth of three coalescence cases with initial radius ratio 1.02, 1.45 and 1.78 obtained from experiment only.

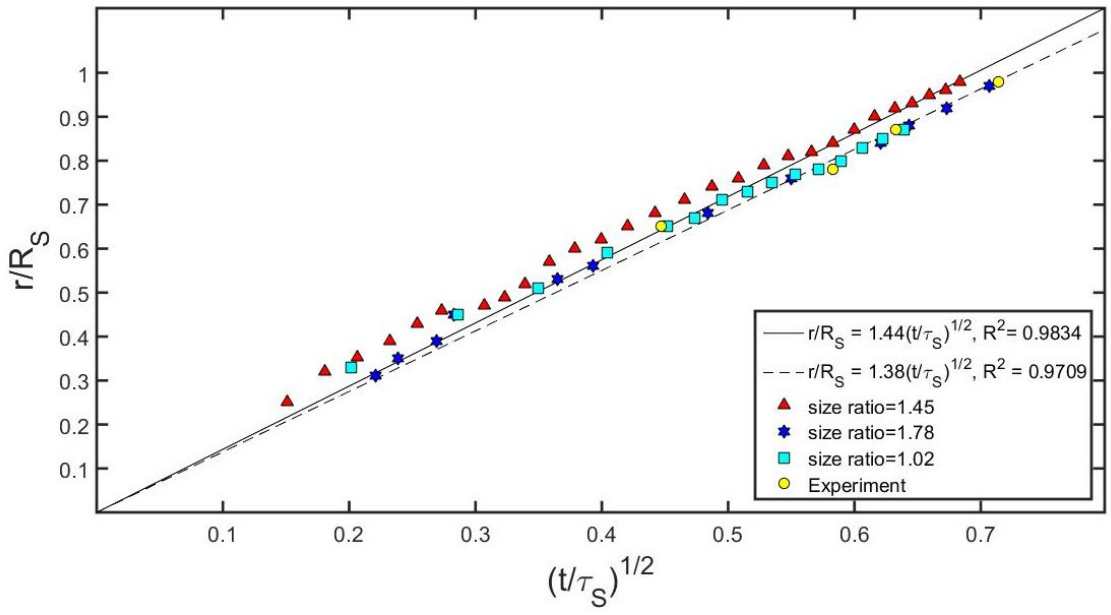

Fig. 2.17. Time evolution of neck growth of three coalescence cases with initial radius ratio 1.02, 1.45 and 1.78 obtained from both experiment and simulation, respectively.

Table 2.2.
Coalescence timescale and radii

Size ratio	$\tau_S/\mu s$	$r_S/\mu m$	$\tau_L/\mu s$	$r_L/\mu m$
1.45	18.95	29	33.03	42
1.02	50.17	55	50.18	56
1.78	26.21	36	62.12	72

As shown in Figure 2.17, the neck growth data from simulation is validated by the four experimental data points. With more data points from simulation, the neck growth still shows a half power-law, $r/R_S \sim 1.44(t/\tau_S)^{1/2}$, with coefficient of determination R^2=0.9834. We can conclude that the neck growth dynamics of two unequal-sized microbubbles captive on a solid surface still shows a half power-law with

the inertial-capillary time scale and controlled by the smaller microbubble regardless the size ratio.

As shown in Figure 2.13, a surface wave starts to propagate along the surface of gas bubble at the initial stage of coalescence. The surface wave or called as capillary wave is driven by the release of surface energy at the neck region. The capillary waves were first formulated as a theory of capillary-gravitational waves for pure liquid case by Kelvin. His theory leaded the simple relationship as:

$$v^2 = g\lambda/2\pi + 2\pi\sigma/\rho\lambda$$

where v is the phase velocity of wave propagation, g is acceleration due to gravity, λ is the wavelength, σ is surface tension, ρ is liquid density. The equation implies that the propagation velocity is determined by gravity for long waves and by surface tension for short waves. The short waves are called capillary or surface waves. [29] A capillary wave to be specified for our microscopic case is a wave traveling along the sphere or boundary of merging microbubbles, whose dynamics and phase velocity are dominated by the effects of surface tension. Capillary waves play a significant role in two microbubble coalescence process generating the after initial touch of microbubbles.

Meanwhile, the Bond number, expressed as

$$Bo = \frac{\Delta\rho g L^2}{\sigma}$$

is a non-dimension number used to measure the importance of gravitational forces contrast to surface tension forces, specifically utilized (along with Morton number, Morton number has the same function but for droplet) to characterize the shape of bubbles or drops moving in a surrounding fluid. Gravity plays a role in all long length scales, while surface tension is most effective at short scales, for instance about 1 cm or less for air bubble in water. [38] For our micro scale case, gravity is temporarily neglected due to

$$Bo = \frac{\Delta\rho g L^2}{\sigma} = \frac{(1060 - 1.2999)kg/m^3 \times 9.81m/s^2 \times (2 \times 56^2 \times (10^{-6})^2 m)}{0.072N/m} = 0.0018$$

which is less than 1, so the gravity effect can be ignored in microscopic scenarios. The capillary wave propagation of velocity v is simplified as:

$$v^2 \sim 2\pi\sigma/\rho\lambda$$

which only related to liquid density ρ, surface tension σ, and wavelength λ. So that surface tension is the only restoring force in the model. One demonstration of the physical understanding that the model gives us is that it provides a simple way to derive the formula for the phase speed of pure capillary waves, propagation angle varying with the phase velocity with constant surface tension.

Wave propagation angle is a way to determine surface wave propagate along bubble surface. As shown in Figure 2.14(b), the propagation angle is measured from the line connecting the centers of two parent microbubbles. Since the wave propagation dynamics is very difficult to capture on the smaller parent microbubble, we focused on the surface wave propagation on the larger parent bubble surface. We obtained surface wave propagation angle data on both experiment and simulation with same conditions mentioned in neck growth evolution. If we only consider the experimental results, the yellow circular markers show a linear relationship between the propagation angle and the time normalized by inertial-capillary time scale. Since the propagation is on the larger parent microbubble, the characteristic length used in the time scale is the radius of the larger parent microbubble. The dash fitting line indicates that $\theta = 3.79(t/\tau_L) + 0.44$, with coefficient of determination R^2=0.9875. If the simulation results are added, a very similar solid fitting is present, $\theta = 3.82(t/\tau_L) + 0.34$, with coefficient of determination R^2=0.9884. Figure 2.18 demonstrates that the surface wave propagation is controlled by the size of larger parent bubble for unequal-sized cased and follows a universal linear relationship with inertial-capillary time scale. However, Figure 2.18 also shows that at the very early stage of coalescence the wave propagation does not follow the same linear law as the later stage. The reason could be due to the release of large surface energy at the very early stage when surface curvature is very large. To explain the surface wave propagation results, a capillary wave theory is used. [39]

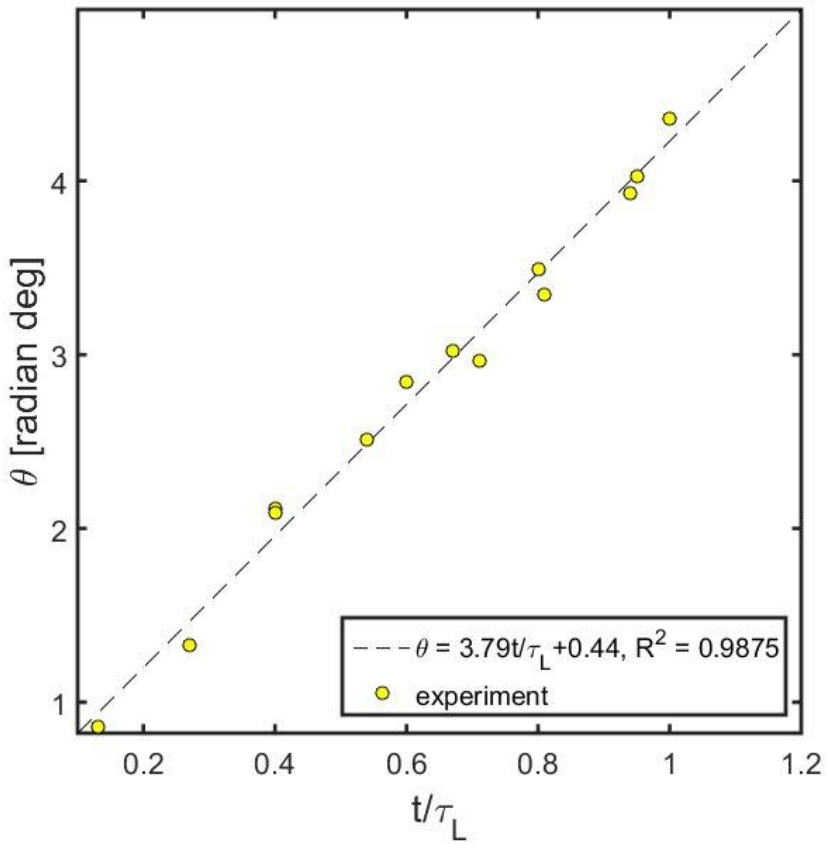

Fig. 2.18. Time evolution of surface wave propagation angle of three coalescence cases with initial radius ratio 1.02, 1.45 and 1.78 obtained from experiment.

When the wavelength λ is short, the wave phase velocity v is proportional to $(2\pi\sigma/\rho\lambda)^{1/2}$, where σ is the surface tension, ρ is the density of liquid. In the bubble coalescence event, capillary wave is the surface wave traveling along the spherical interface of merging bubbles. If we consider that the wavelength is proportional to the radius of the microbubble, the propagation angle $\theta \sim t/R_L = t(2\pi\sigma/\rho R_L^3)^{1/2}$. Then $\theta \sim A(t/\tau_L)$, where $\tau_L = (\rho R_L^3/\sigma)^{1/2}$.

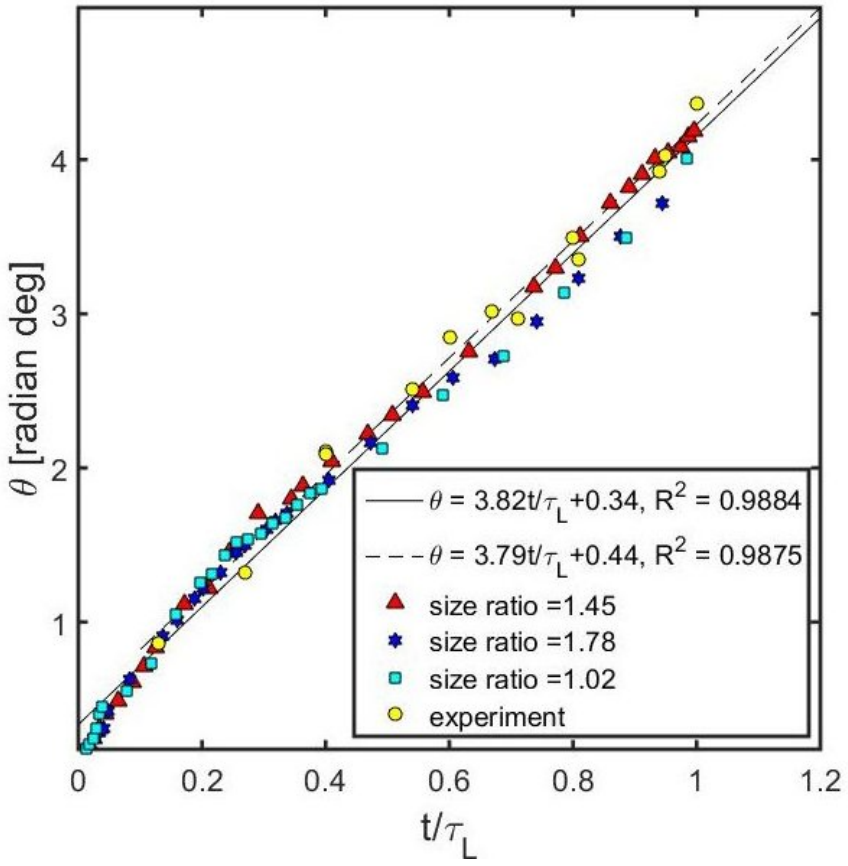

Fig. 2.19. Time evolution of surface wave propagation angle of three coalescence cases with initial radius ratio 1.02, 1.45 and 1.78 obtained from experiment and simulation. Dash line and solid line are the fitting lines from both experiment and simulation, respectively.

2.3.3 Neck Growth and Surface Wave Propagation Study on Contact Angle Effect

The neck growth during merged bubble formation is complex with several characteristic parameters. [40] The above conclusion on neck growth and surface wave propagation study are based on the scenario when microbubbles are attached on solid interface with a contact angle as 36 °. We simulate microbubble pair coalescence with different contact angle on solid interface to obtain an better understanding of how contact angle affects the neck growth formation and surface wave propagation.

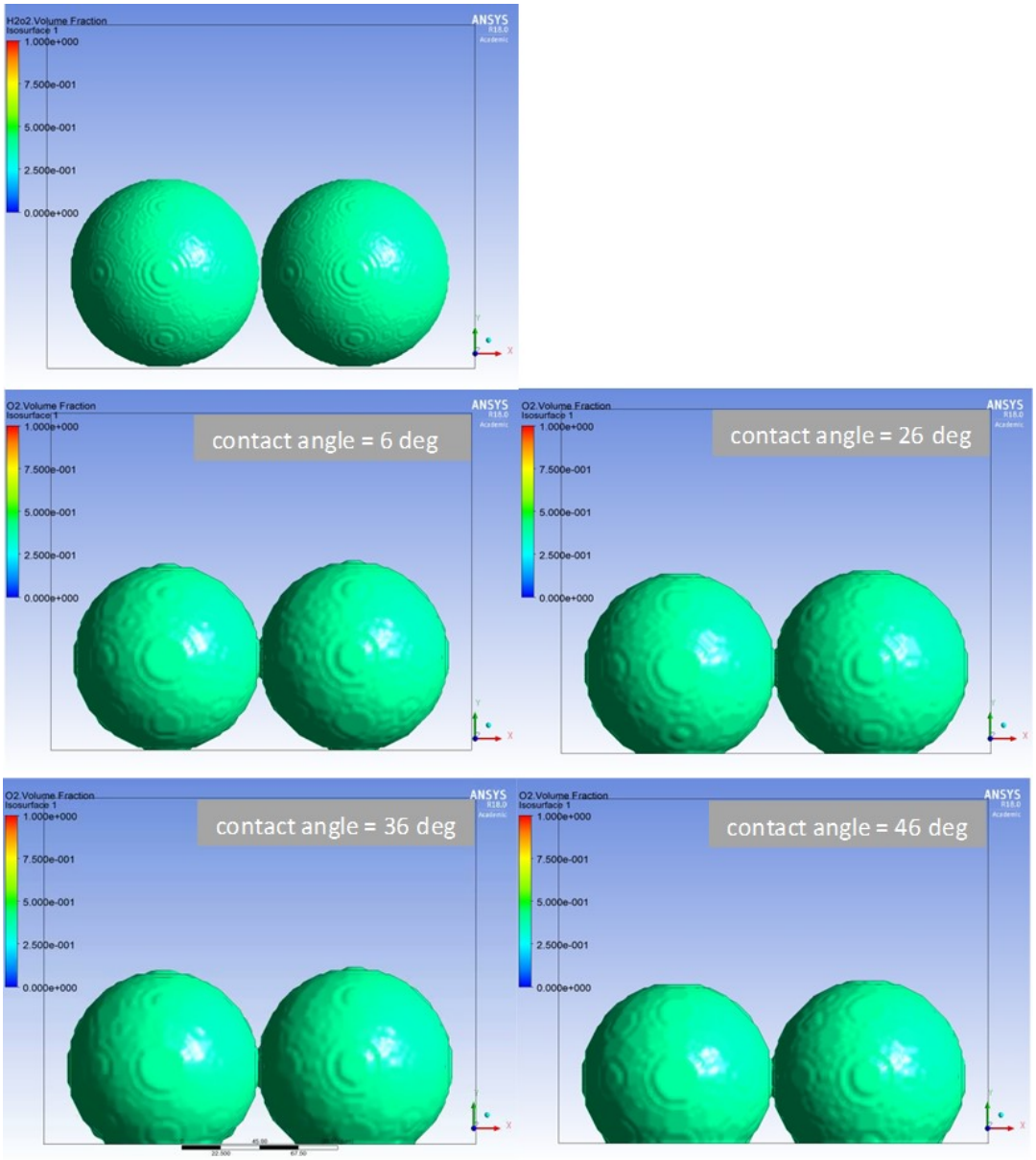

Fig. 2.20. Time evolution of neck growth of five coalescence cases with contact angle 46°, 36°, 26°, 6° and 0 ° obtained from simulation. Dash line and solid line are the fitting lines from both experiment and simulation, respectively.

Owing that ANSYS FLUENT allows us conduct coalescence simulation without any observation and measurement constrain. The 3D modeling is employed of equal-sized ratio microbubble doublet, contact angle ranging respectively 0 °, 6°, 26°, 36°

as well as 46° in Figure 2.20. Meanwhile similar measurement approach of ImageJ attained the relationship $r/R \sim (t/\tau)^{1/2}$ and $\theta \sim (t/\tau)$ by fitting the half-power-law curve $r/R = 1.41(t/\tau)^{1/2}, R^2 = 0.9553$ and $\theta = 3.58(t/\tau) + 0.45, R^2 = 0.9758$ shown in Figure 2.21 and 2.22, respectively. That demonstrates different contact angle, precisely, different solid-liquid state intersection between microbubble and ground do not affect the evolution of bridging neck growth and surface wave propagation in the early stage of coalescence. The potential explanation is the part below center of microbubbles is not involved in the initial conjunction process of microbubble boundaries.

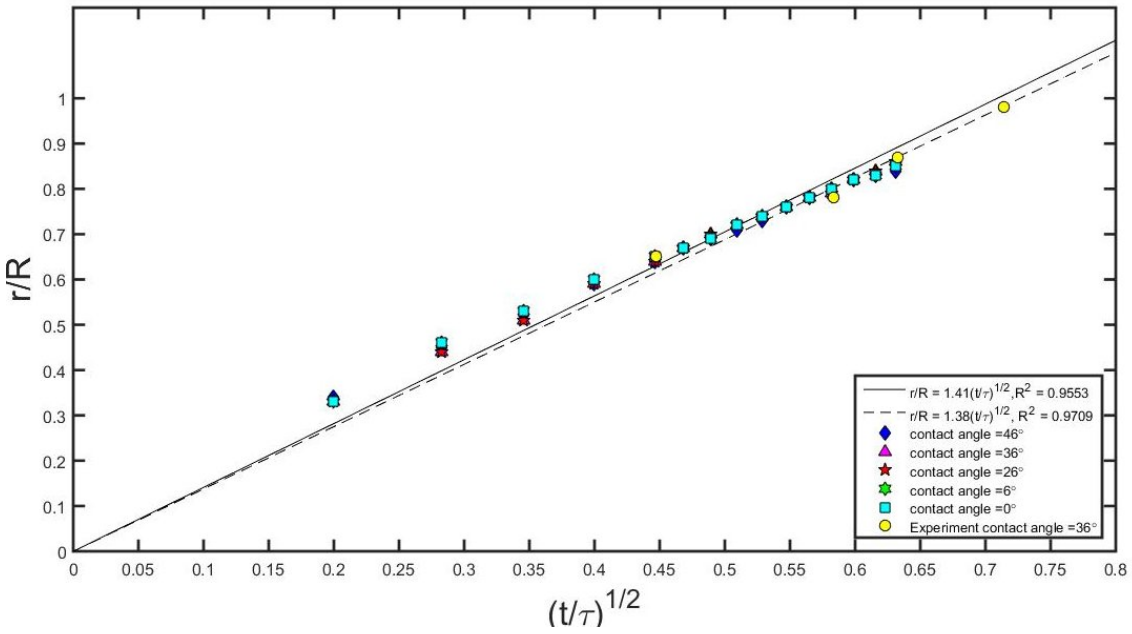

Fig. 2.21. Time evolution of neck growth of five coalescence cases with contact angle 46°, 36°, 26° , 6° and 0 ° are from simulation. Dash line and solid line are the fitting lines from both experiment and simulation, respectively.

Since that, we deployed 2D simulation on coalescence with no contact angle or free in solution. We set the microbubble pairs pendant, free in the H_2O_2 solution see Figure 2.23 keep centers of microbubble in a line.The size ratio of them are 1.0, 1.45, 1.60, 1.78, and 3.0.

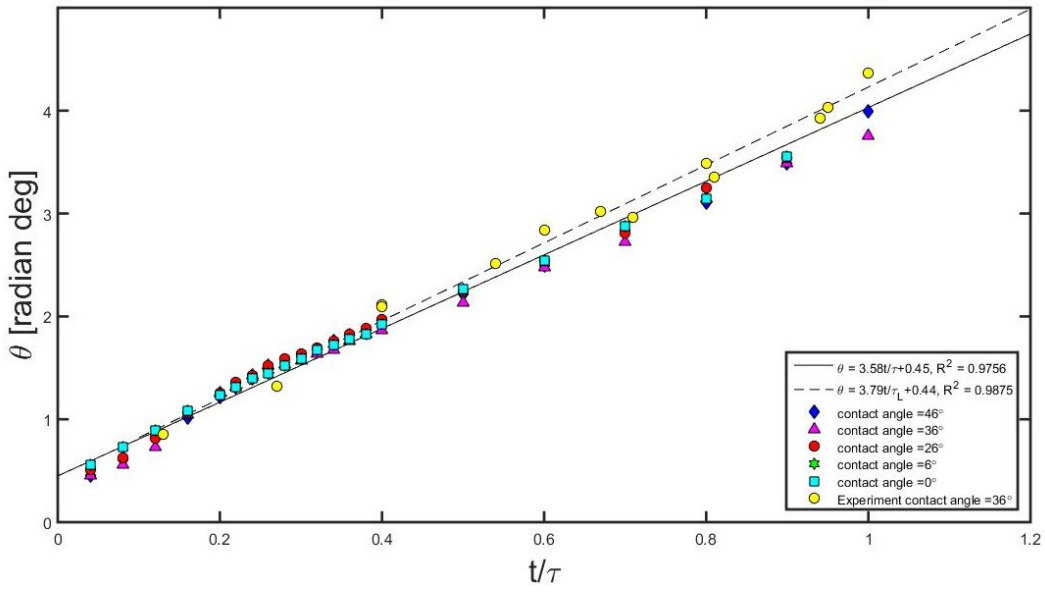

Fig. 2.22. Time evolution of surface wave propagation angle of five coalescence cases with contact angle 46°, 36°, 26° , 6° and 0 ° are from simulation. Dash line and solid line are the fitting lines from both experiment and simulation, respectively.

We want to see if the size ratio would influence the neck growth, while applied the experimental microbubble merging cases as a contrast group. The results are outlined as following Figure 2.24. The solid line $r/R_S = 1.35(t/\tau_S)^{0.5}, R^2 = 0.9871$ in Figure 2.24, follows the half-power-law relation between time evolution and bridging neck growth before parent microbubbles merge into one. Clarified for our case, we used not only the equal-sized microbubble pair but also the unequal-sized pair. Thus specifically, the neck growth evolution is governed by the smaller bubble due to no bridge conjunction exists, after separate microbubbles merging into a single one.

Compared with 3D modeling, we find that 2D modeling has much advantages under the conditions that contact angle unable to sway neck growth and surface wave propagation. It does not cost much calculation time as 3D modeling does and allows less governing boundary conditions to smooth mesh and simulation.

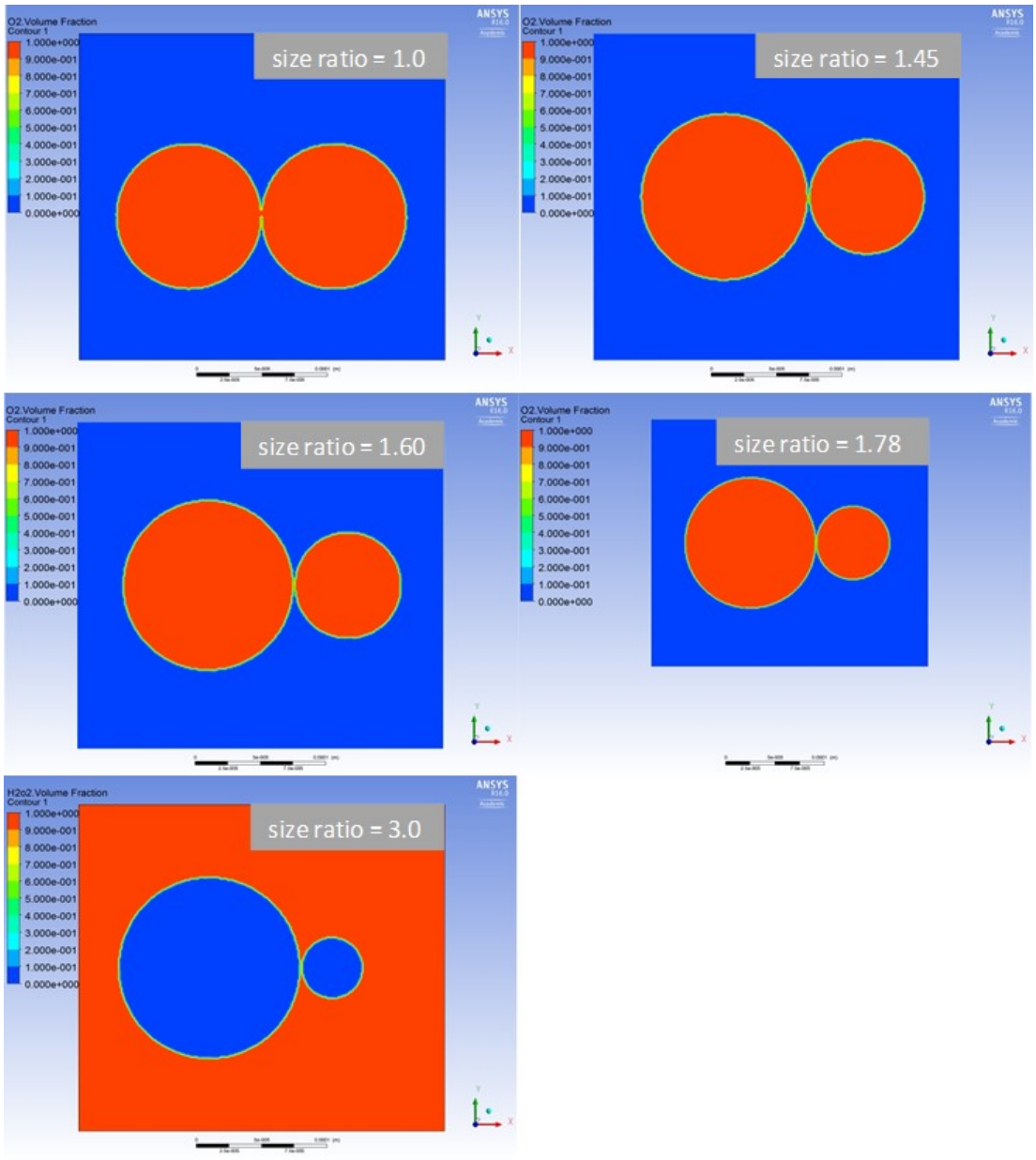

Fig. 2.23. 2D microbubble coalescence modeling and initial state of microbubble pair was pendant in liquid solution.

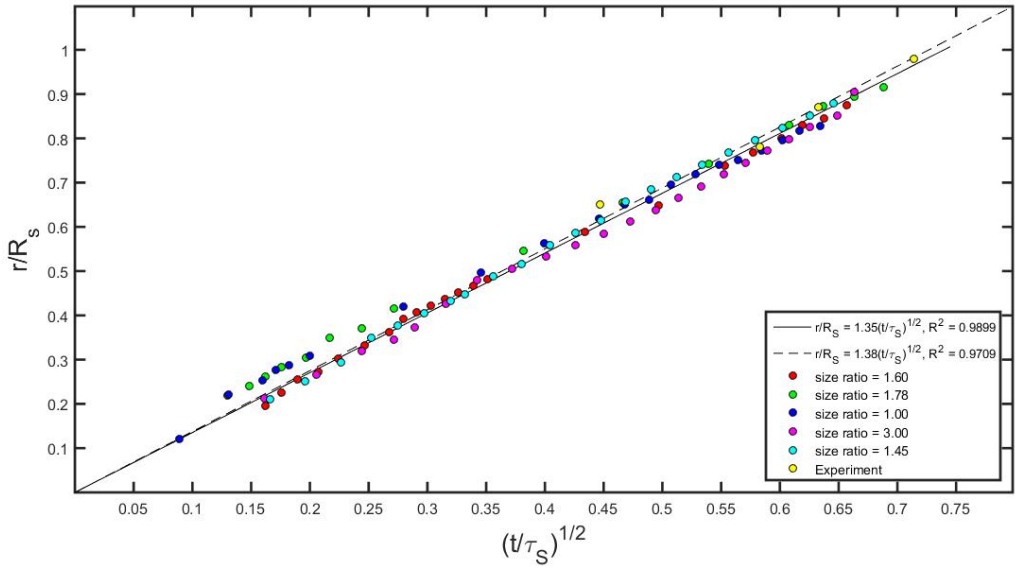

Fig. 2.24. Free microbubble 2D modeling represents linear relation between neck growth coalescence timescale.

2.4 Conclusion

In this chapter, the neck growth and surface wave propagation in the early stage of coalescence of unequal-sized microbubbles captive on solid substrate were investigated experimentally and numerically. A special polymer microfluidic device was designed and fabricated to generate microbubbles and coalescence events. The high-speed X-ray imaging instrument at the 32-ID-B beamline of the Advanced Photon Source at the Argonne National Laboratory was utilized to visualize individual coalescence events in the microchannel from the cross-section view at 10^5 fps frame rate.

The image analysis show that the neck growth dynamics of two unequal-sized microbubbles captive on a solid surface shows a half power-law with inertial-capillary time scale and controlled by the smaller parent microbubble. The surface wave prop-

agation on the larger parent microbubble follows a universal linear law with inertial-capillary time scale. The relationship between

$$r/R_S \propto (t/\tau_S)^{1/2}$$

matches the analytical solution provided by Paulsen, et al. [15] We combine the results of experiment about neck growth with results of simulation. Found that they largely are in the same fitting line, which confirms the convergence of simulation. The tendency of capillary wave propagation angle and coalescence timescale $(t/\tau_L)^{1/2}$ is linearly related. We combine the results of experiment about propagation angle variation with results of simulation. Found that they largely are in the same fitting line, which confirms the convergence of simulation.

The neck growth variation is basically dominated by the smaller bubble in the coalescence pair. While as for capillary wave propagation angle is determined by the larger bubble after microbubble pair merging into a single merged one. The contact angle caused by solid interface and liquid surrounding microbubble, would not have an effect on the merging boundaries of microbubble.

3. STUDY ON PREFERENTIAL DISTANCE OF MICROBUBBLE COALESCENCE

3.1 Introduction

Microbubble commonly defined as a bubble of diameter range from 1 micrometer to 1000 micrometer1, has promising and wide applications in biological, chemical and medical areas, such as active substance for water treatments, ultrasound agents targeted for drug delivery or gene/DNA tracking and ultrasound imaging Numerous composition of shell and filling materials impart researchers much more possibility to find better design properties of microbubble, like buoyancy, crush strength, thermal conductivity, and acoustics. Coalescence, one of intricate microbubble dynamics phenomena, has attracted scientific interests since nearly century, yet constrained by the observation device and bubble generator, researchers do not have a comprehensive understanding of the physics. The coalescence process—the tendency for two touching spheres to form a single larger sphere—occurs as a result of the surface energy minimization and is supposed to take place at various condition, for instance, microbubbles sessile or free with substrate in liquid solution, centers of the them could be in the same line or else not.In coalescence dynamics, the size inequality of the parent bubbles plays a significant role in mass transport and topological change [2] due to the pressure difference, also called Laplace difference between bubbles. As a larger size parent microbubble induces a larger pressure difference and helps overcome larger viscous stresses so that it is conceivable that the pressure difference created by the size inequality would cause a merged sphere to be preferentially oriented toward a larger parent sphere. [23] Then a bubble merged from two parent bubbles with different size tends to be placed closer to the larger parent. Most previous experimental and numerical studies of bubble coalescence confirmed this theory via power-law

functions of various exponents, based on cases of that merging bubble pairs are in a same center line and free in solution. However, sufficient observation on cases of that microbubbles are sessile with a specific solid interface in liquid and the centers of them are not coaxial is still covered. [22]

In this chapter, we provide experimental confirmation of coalescence preference in the scenario that microbubbles were contacted with solid substrate and entrapped inside a channel. We demonstrate that this preference distance is a function of the parent size ratio through high speed X-ray synchrotron imaging analysis of coalescing oxygen microbubble pairs sessile on solid interface in 30% hydrogen peroxide solution. Our main results show that the merged bubble position is largely dependent upon the parent size ratio r_L/r_S: as the ratio increases, the merged sphere position becomes closer to the larger parent position.

3.2 Experimental

The same imaging acquisition technology was applied as Chapter 2. Details on experiment setup and cross- section view observation was mentioned in the same position of Chapter 2.

Taking advantage of synchrotron X-ray facility, allows outline of bubbles, either overlapped or contacted was clearly identified. The flow run from inlet through check valve, the gas bubbles propagating on the solid substrate transferred to gas vent by membrane due to pressure difference.

High speed phase-contrasting images were caught from the cross-section of gas generator to observe and analyze the behavior of merging bubbles during the self-regulating gas generating process in the device. The microbubbles (O_2 bubble) were generated consecutively during the reaction of hydrogen peroxide (30% H_2O_2) with Pt catalyst, and meanwhile the hydrophilic channel would not stock bubbles so that we found bubble pairs merging properly inside the channel. The resolution we set for

camera of synchrotron facility was 320 × 128 pixel, and the length of each pixel is represented for 2 μm. [5]

3.3 Results and Discussion

The benefits of synchrotron X-ray imaging facility, high-speed, high-resolution and intense microscopy, aided us to capture distinctly visualized cross-section view of coalescence dynamics through the microfluidic gas generator. While traditional optical technique utilized by previous experimental studies was not capable to reach this, details can be found in Chapter 2 and Figure 2.13 and 2.14.

Table 3.1.
Microbubble cases with different radius ratio

Case No.	Radius ratio(R_L/R_s)	$R_L/\mu m$	$R_S/\mu m$	$R_M/\mu m$
1	1.56	42	27	46
2	1.37	26	19	30
3	1.80	45	25	48
4	1.45	42	29	45
5	1.09	48	44	58
6	1.02	56	55	70
7	1.78	64	36	68

There are seven merging cases eligible for microbubble coalescence study (see Table 3.1 below). A representative image sequence of bubbles captive on the interface in 30 % H_2O_2 solution is given in Figure 3.1. Here the individual profile of oxygen bubbles in each frame was distinctly captured at a frame rate of 100 KHz (10 μs per frame) via ultrafast camera. We can see that at 0 μs, two parent bubbles were about to contact each other. The contact boundaries disappearing took place less than 10 μs, as soon as the two bubble have formed the joint meniscus at 10 μs, with a partial

saddle in the middle bridge. The formation of this bridge demonstrates the growth of initial effect on coalescence process. [22] Since the bubble merging happened very fast, and with the merging of two bubbles into one bubble, the peripheral parameters of the bubbles also needed to change and rearrange accordingly, including the total surface area, volume of the bubbles and surface energy. This sudden motion provided relative high kinetic energy for the bubbles, therefore enabling a series of oscillating movement for the merged bubble, which can be observed at 20 - 130 μs frame points. It is noticed that each of these frame, even though only has short time step of 10 μs, possesses obvious bubble shape difference. This indicates high kinetic energy of the bubble after the merging, and the energy was dissipated to the peripheral environment through the bouncing-like activity. The formation of the new sphere initiated drastically from the right outer boundary of smaller parent bubble whereas the left outer boundary of larger parent bubble was reformed late after. Kinetic energy of the new merged bubble was transmitted from right side to left side until each side reached balance state (see image sequence in Figure 3.1).

While the equal-sized microbubbles remain the symmetrical shape through merging process. Initially microbubble pair transformed from which the walls once separating them go flat and then grow up to a peak vertically, meanwhile the new merged periphery horizontally go down until bulging of each side arises. Then the meniscus outline changed into oblate ellipse along y axis, finally become a new sphere appear (see image sequence in Figure 3.1).

3.3.1 Coalescence Preference Distance

To further understand the insight physics of microbubble coalescence, we delineated the geometric relation of parent microbubble pair with the merged one by simplifying an unequal-sized coalescence case as a schematic view shown in Figure 3.2. $a_L(a_S)$ is defined as the distance from larger (smaller) parent center to the shortest point on the line connecting the parent centers to the merged center. [23] The

sphere of bubbles plotted in the Figure 3.2 was partial as we did not ignore the effect of solid interface during coalescence process, using ImageJ, a public domain, Java-based image processing program developed at the National Institutes of Health. A triangle in Figure 3.2 consisting of the corners that link the centers of parent bubbles and daughter bubbles enabled us to evaluate the relative position a_L/a_S. d_L and d_S denote the horizontal distance from centers of parent bubble to the merged one respectively. The ratio of d_L and d_S is regarded as the coalescence preference distance. For our case, we take the confirmation of $(r_M)^3 = (r_L)^3 + (r_S)^3$ which is simplified from mass conservation of bubbles negligible constant coefficient, given $m = \rho V$, $V = (1 + 2cos\theta)\pi r^3$, $\rho = 1.3Kg/m^3$, and the contact angle θ is 36° taking and solid substrate effect into account instead.

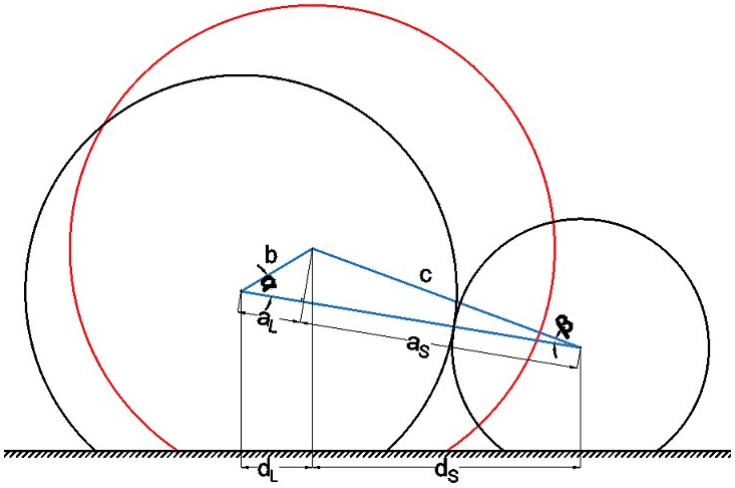

Fig. 3.1. Schematic view of coalescence preference geometry. The relative position of the merged bubble is measured through the relations $a = a_L + a_S$ and the side lengths a, b, and c as a function of the parent radius.

We used to convert size of each image frames to its actual size given each pixel is 2 μm long and easily to know the diameter of bubbles. Owing to pixels, cant be measured as a slope, we applied the angle α, β to obtain the lengths of b and c which

can be calculated directly via ImageJ after Pythagorean theorem of horizontal and vertical distance from parent bubble centers to the merged center.

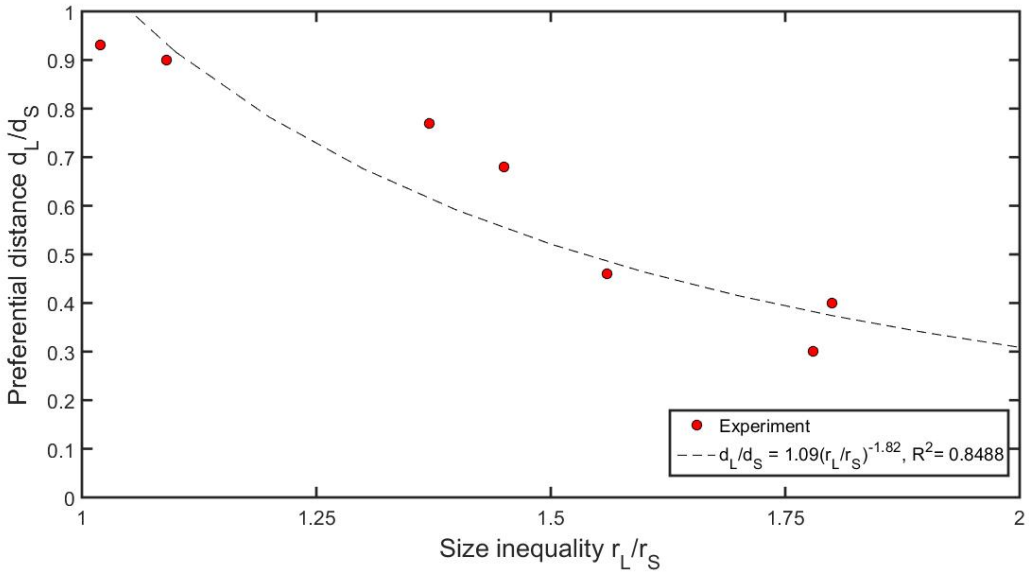

Fig. 3.2. Coalescence preference relation of r_L/r_S and d_L/d_S.

Given three important geometric constraints for coalescence case: (i) all spheres contact the ground interface (ii) $(r_M)^3 = (r_L)^3 + (r_S)^3$, and (iii) $a = a_L + a_S = r_L + r_S$. [22] The lengths of a_L and a_S are determined by $cos\beta = (a^2 + c^2 - b^2)/2ac = a_S/c$, $cos\alpha = (a^2 + b^2 - c^2)/2ab = a_L/c$, so the relative position a_L/a_S can be expressed as: $a_L/a_S = (a^2 + b^2 - c^2)/(a^2 + c^2 - b^2)$ The relative position a_L/a_S is a function of the parent size ratio r_L/r_S, since a, b and c are functions of r_L/r_S so that in these cases, $(a_L/a_S) \sim (d_L/d_S)$ illustrated in Figure 3.3 which demonstrates that the relative position a_L/a_S can be matched through coalescence preference distance d_L/d_S linearly with a trend line $y = 0.98x - 0.02$ displayed on Figure 3.4 and R-square value $R^2 = 0.9956$.

The relative position a_L/a_S is a function of the parent size ratio r_L/r_S, and $(a_L/a_S) \sim (d_L/d_S)$, hence preference distance d_L/d_S is highly dependent on parent

bubble of size inequality shown in Figure 3.3. This results verifies the suppose that the merged bubble becomes closer to the larger parent bubble that means ratio d_L/d_S decreases when the parent size inequality ratio r_L/r_S increases. The power-law relation $d_L/d_S = m(r_L/r_S)^{(-n)}$ between d_L/d_S and r_L/r_S with an exponent $n = 1.82$ and $m = 1.09$, R-square value $R^2 = 0.8488$. This power-law relationship was specialized for the case of that gas bubble captive on ground channel interface, emphasizing surface tension effect, contrast with previous microbubble unattached merging in liquid solution.

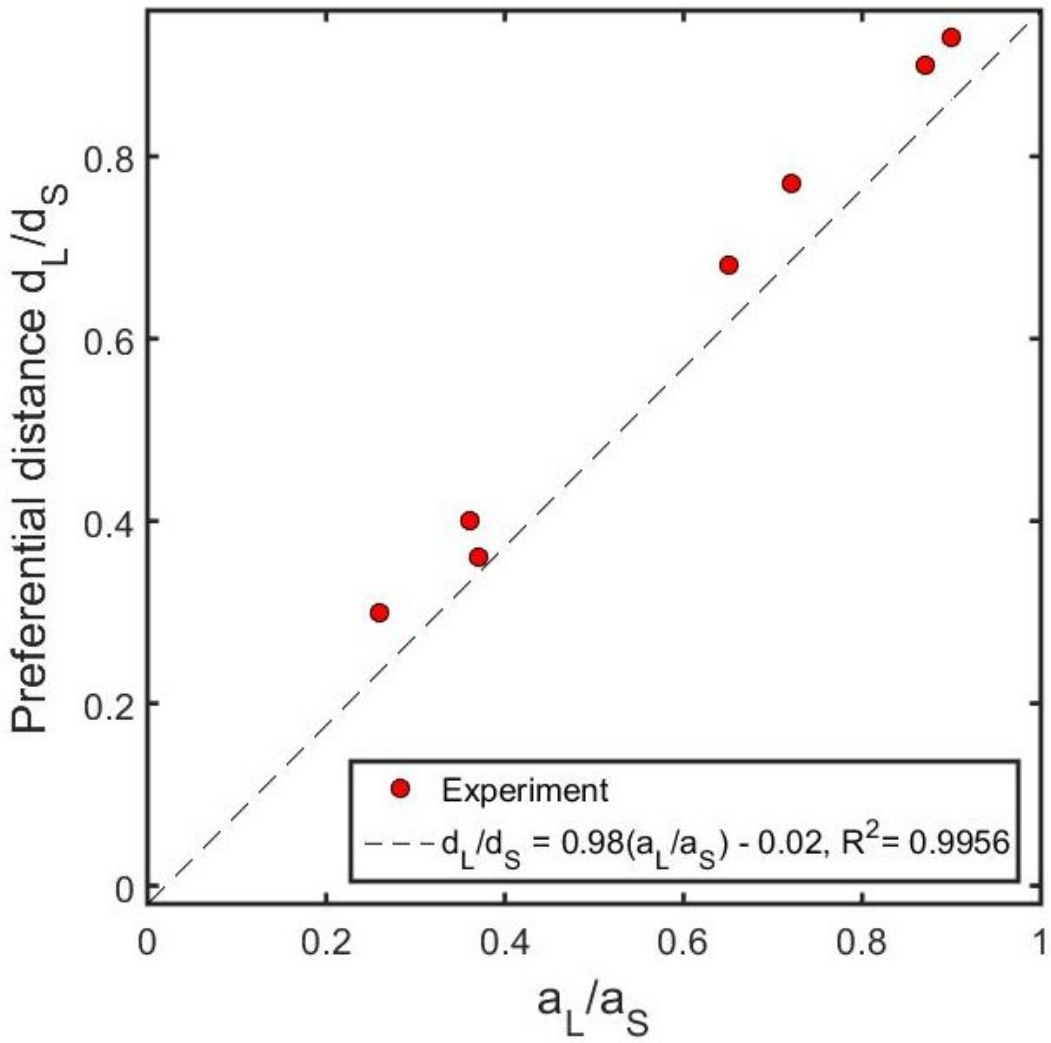

Fig. 3.3. Relation of d_L/d_S and a_L/a_S.

There is a prevailing theory for free bubble coalescence in water similar to our results, on the respective of surface energy transformation. As is mentioned that for an ideal case that gas bubble on ground interface but gravity and surface effect is ignored, the mass movement to the position of the merged sphere (a_L or a_S) would be proportional to the kinetic energy (k) gained from the surface energy difference (surface energy referred to $S = \sigma \Delta s$, s is the area of sphere), between the parent and the merged spheres. The relative kinetic energy accords to the fraction of the surface energy difference as for the large parent and for the small parent [4]. We know that $k_L/k_S \sim a_L/a_S$. Also the kinetic energy ratio k_L/k_S is given as,

$$(k_L/k_S) = ((S_M - S_L)/S_L)/((S_M - S_S)/S_S) \approx (r_L/r_S)^{(-5.3)}$$

suggesting that the coalescence preference is controlled by the topological change by the energy release. Compared with the theoretical exponent n=5.3 of the power-law function with our n=1.82, the exponent difference indicates that in our case, after parent bubble coalescence, the new formed sphere is less closer the larger parent bubble, or may be more closer to the smaller parent bubble.

3.3.2 Wall Shear Stress Analysis

To reconcile our results with the theory is adding surface tension effect of the solid substrate into account. As the regime for two gas sphere merging into one credits to the Laplace pressure difference Δp, $\Delta p = 2\gamma(\frac{1}{r_s} - \frac{1}{r_L})$, the gas from smaller bubble moves strongly forward to the larger one in an ideal circumstance. We propose a scenario that during merging process, a drag or friction between flow and solid interface will give rise to a force resisting relative motion of parent bubbles. The force F, $F = \mu A dv/dy$, v the flow velocity along x lateral direction and y-axis perpendicular to flow, μ referred as dynamic viscosity, is found to be proportional to the speed v and the area A of contact section on substrate, and inversely proportional to their separation y.

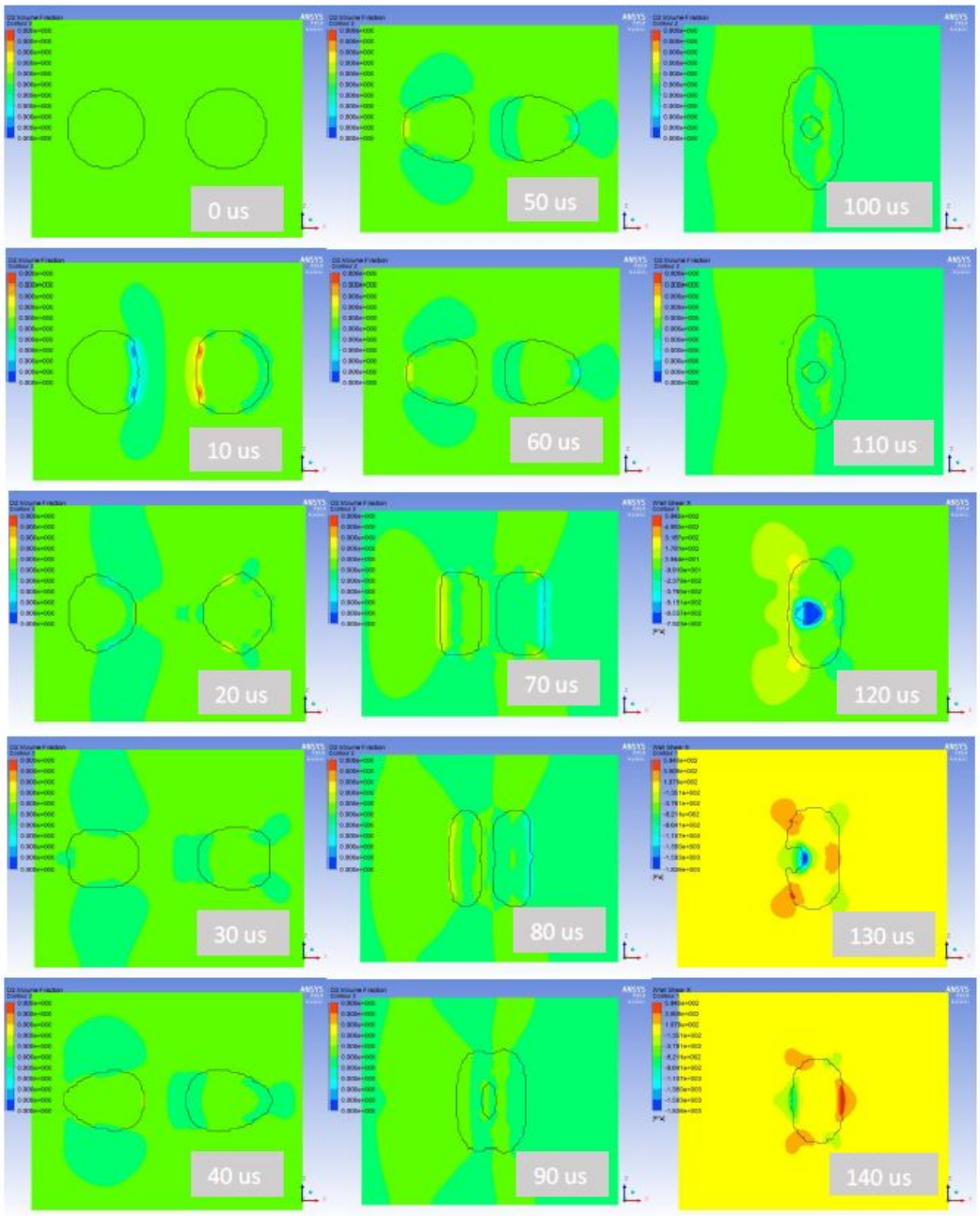

Fig. 3.4. Wall shear stress contour of 3D equal-sized microbubble during merging. The interval of each figure is 10 μs same as the one in experiment.

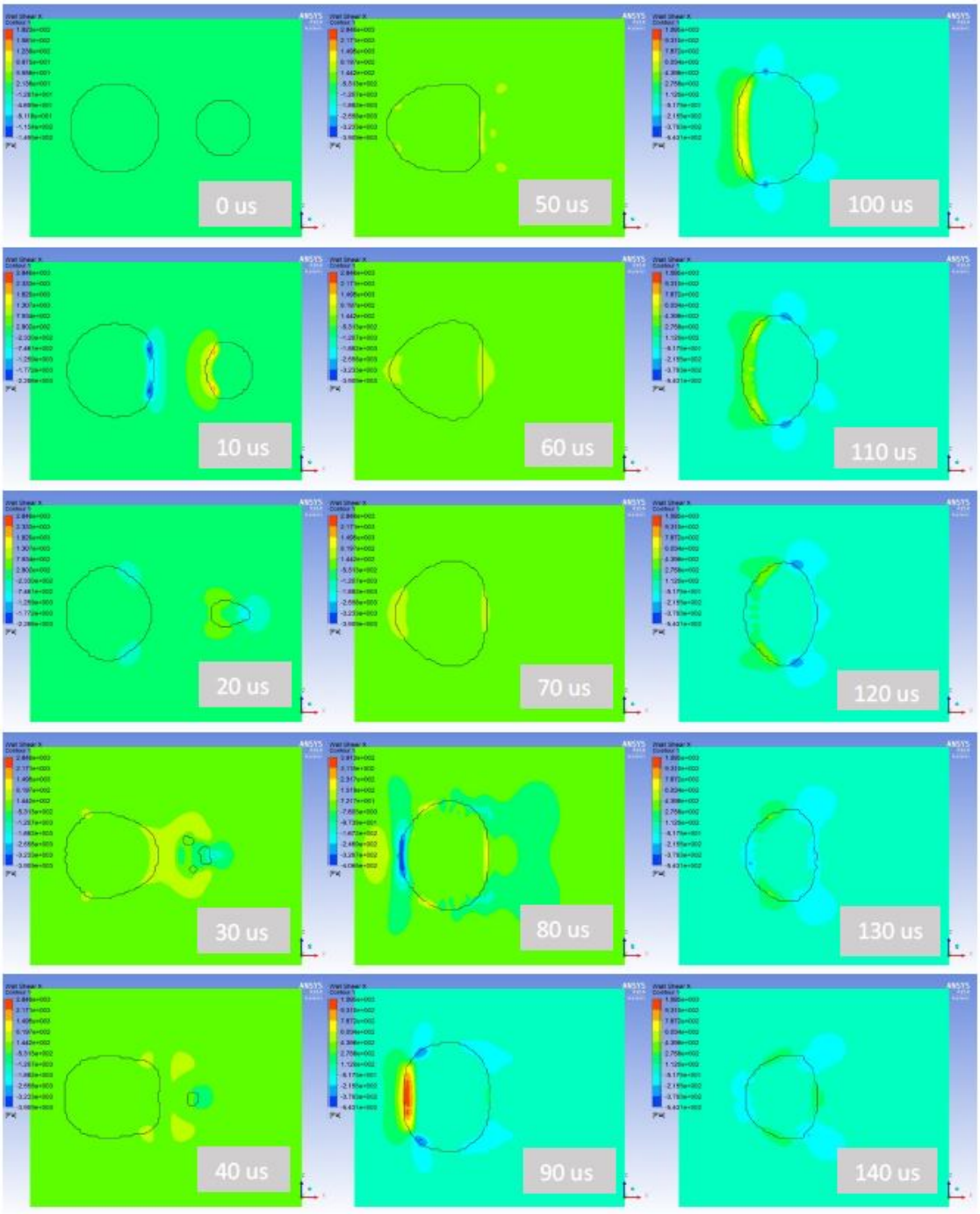

Fig. 3.5. Wall shear stress contour of 3D unequal-sized microbubble during merging. The interval of each figure is 10 μs same as the one in experiment.

Wall shear stress $\tau_w = \mu dv/dy$, where $\tau_w = F/A$, acted oppositely on the bubble pair to hindering formation movement along the solid interface the merging progress in our case. Intensely the wall shear stress of the solid interface reduced the displacement of the born bubble, being a potential cause to explain our results.

The purpose of wall shear stress analysis is to aid our explanation on preference distance of microbubble coalescence mentioned and Figure 3.5 and 3.6 depict the wall shear stress contour on the solid ground along the x direction. The legend right in the Figure 3.5 and 3.6 shown the qualitative variation of wall shear stress along lateral direction. From 0 to $20\mu s$, the small bubble has larger wall shear stress to hinder the movement towards to the larger one. Meanwhile from 50 to 80 μs, the stress on right side of larger bubble obstruct the its boundary reaching the smaller one. From 90 to 110 μs, the stress on left side of larger bubble obstruct the its boundary reaching the smaller one. Wall shear stress $\tau_w = \mu dv/dy$, where $\tau_w = F/A$, acted oppositely on the bubble pair to hindering formation movement along the solid interface the merging progress in our case. Intensely the wall shear stress of the solid interface reduced the displacement of the merging bubble, which confirms our explanation of results.

3.3.3 Displacement of Contact Point

Besides the analysis on preference distance of merging microbubble pair, we aware that the microbubble's sphere was cut off by the solid surface, like a spherical dome, due to surface tension effect. The purpose of this study is to learn about the motion tendency of merging microbubble pair sessile on a solid surface. Schematic view of measurement on the offset distance of contact point is illustrated as Figure 3.7 with red solid circle marker. The movement of two farthest points on the contact dome with ground presents the dynamics of coalescence. The distance along lateral direction from the right or left contacting point to the line through center of merged microbubble is regards as the displacement of contacting point.

We define that positive movement of contact point is that of larger microbubble forwarding right to the center line of merged microbubble as l_L, verse vice–minus movement of the point at the smaller microbubble side as l_S. Figure 3.8 and 3.9 presents two different size ratio microbubble pair during coalescence process, the contact point change along lateral direction.

The equal-sized microbubble pair, merging details mentioned above (see Figure 3.1) point out the new merged microbubble was at the midst two forming microbubble transversely. The change of each contact point occurs simultaneously, dramatically at initial and then calm down to small damping (Figure 3.8). While for unequal-sized microbubble pair, we find large movement discrepancy on the smaller microbubble side and once the pair merged into one comparative round sphere, the tendency of movement keeps consistent (see Figure 3.9). The new born microbubble was supposed to be closer to the larger merging one.

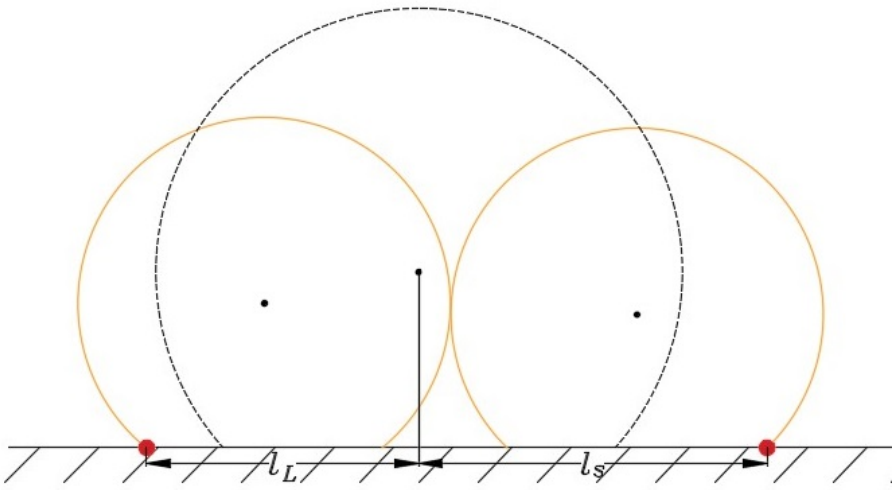

Fig. 3.6. Schematic view of measurement on displacement of contact point.

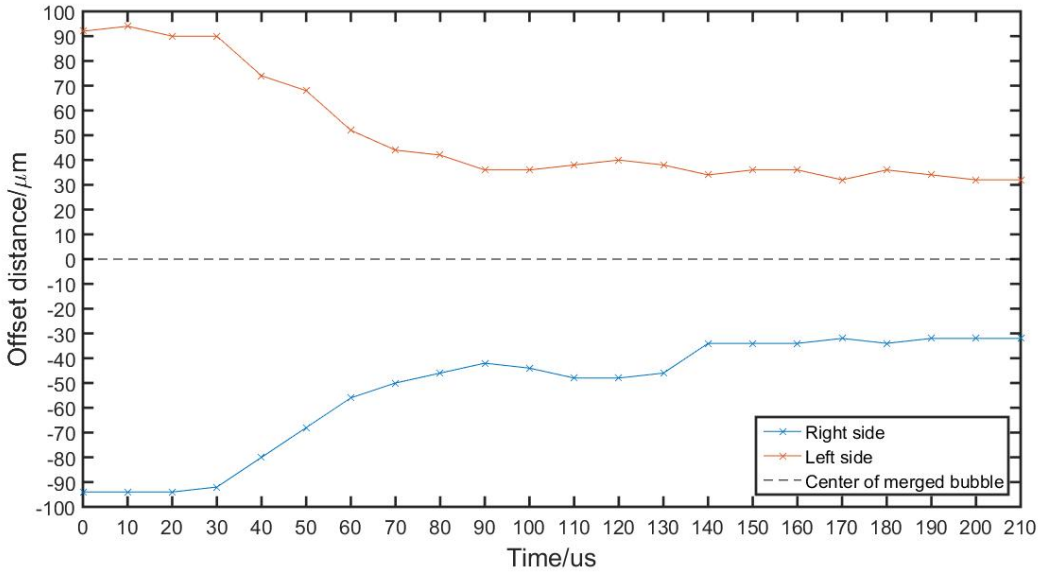

Fig. 3.7. Displacement of contacting point of equal-sized microbubble pair. The orange solid line and cross present the positive farthest distance as l_L from left side normally the larger microbubble to the center line of merged bubble. The blue solid line and cross present the negative farthest distance as l_S from right side normally the smaller microbubble to the center line of merged bubble.

3.4 Conclusion

We state series of case study concerning the coalescence preference distance in microbubbles captive on the substrate inside a microscale channel. Our study provides a more detailed individual visualized microbubble coalescence contrast to previous research, and In particular, high-speed high-resolution synchrotron X-ray microscopy is much useful to provide the key evidence by taking the individual coalescence events from microbubbles sessile on the substrate inside the channel. The geometric relation between the relative coalescence position and the parent size ratio clearly demonstrates that the coalescence may follow a power-law relation with an exponent n=1.82, which was expected for free bubble to be 5.3 in theory.

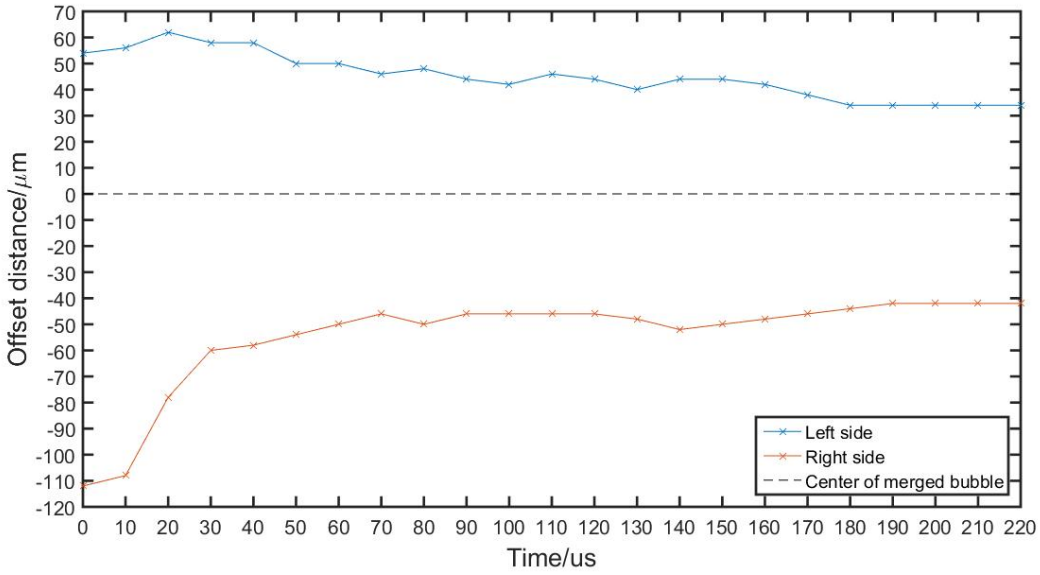

Fig. 3.8. Displacement of contacting point of unequal-sized microbubble pair. The blue solid line and cross present the positive farthest distance as l_L from left side normally the larger microbubble to the center line of merged bubble. The orange solid line and cross present the negative farthest distance as l_S from right side normally the smaller microbubble to the center line of merged bubble..

Our results and analysis show that after merging the horizontal preference position of the new sphere can be placed less closer to the larger parent bubble. The power-law of relative position a_L/a_S and bubble size inequality d_L/d_S in this case is quite different from that surface energy theory given for free bubbles that are not confined in channel and attached on a solid interface. We believe that this result would be important to understand the coalescence dynamics under different situations and further study on surface energy released between solid interface and liquid interface. Additionally, the partial study on displacement of contacting points has representative the microbubble pair shifting movement on the ground.

4. MICROFLUIDIC GAS GENERATOR CHANNEL OPTIMIZATION

4.1 Introduction

Microfluidic system has become a distinct novel field with manipulation from 10^{-9} to 10^{-6} liters of fluid in multiple channels. The field of microfluidics origins from four related area of study: molecular analysis, biodefence, molecular biology and microelectronics. The advanced development of microfluidics due to the research requirements first emerged, which lies in several micro-analytical methods gas-phase chromatography, high-pressure liquid chromatography and capillary electrophoresis. High sensitivity and high resolution property is supposed to be achieved by these methods meanwhile with the use of the laser in optical detection. Applying very small amounts of sample for initial application in chemistry and biochemistry area. Then With the accomplishment and utility of these micro-analytical methods, researchers enable the development of advanced, more compact and more versatile formats microfluidic channel, and to look for other applications for further commercialization. [41]

The following areas, chemical material synthesis, biological medicine analysis, optics and information technology are influenced directly by the evolution of microfluidics. However the field is still at its early phase of development even applications were widespread used in research and industrial area. Due to the basic science and technological facilities develop slowly, problems on selection of initial applications, developing tactics must be addressed to complete for cycle of development, including commercialization. The solutions to these problems will require the innovation and consistent research of work. [42]

In the last decade, the progressive expansion of microfluidic applications arose plenty of research works. A few previous microfluidic appliance were invented on complicated fabrication procedures, such as photo-lithography technology on silicon layers, hot embossing and injection molding on polymer materials, and direct machining using CNC or milling machine. High quality devices were usually manufactured by the fabrication methods mentioned above. However, to use these methods, expensive equipment and long fabrication term, are companied with low resolution. [41]

A commanding prospective for portable biological assays is implemented by the growth of microfluidic system. [41,43,44] In microfluidic area, diverse chip-implanted micro-channels allow small volumes of solution, sample, and reactants, move through. Sorts of biological and biomedical assays show the tendency that shrink varies bio-assays, for instance, DNA sequencing, cell coalescence and enzymatic reaction into a chip format. The benefit of miniature versions of bio-assays not only provides capability of rearrangement of bio-assays but also, requires small amount of solutions, reactants, and cells, short reaction period, portability, less cost, less consumption of power than conventional bio-assays, and diversity in design. With the development of microfluidics, the potential for parallel control and integration with other miniaturized devices should be achieved shortly. [45]

This chapter introduces an updated work of microfluidic gas generator to obtain a better gas generation performance. Previous research of Dr. Likun Zhu's group, stated the basic idea of this chapter in the paper, "Development of A Microfluidic Gas Generator from An Efficient Film-based Microfabrication Method". An advanced PS film integrated fabrication method developed by Yuanzhi Cao was employed to manufacture the device.

By using the polystyrene (PS) films and thermal press bonding process, fabricating the device, our goal is not only to know about the mechanism of self-regulating and self-circulating, but also to enhance the parameters affecting gas generation. Known that the channel dimensions as the essential factors to determine the performance of device, this time we are focusing on the optimization devices with multiple channel

designs to obtain a better testing performance, gas generation rate and reactant solution rate, of the gas generator. We have been fabricating the device with multiple channel arrangements (parallel). The parallel design aims to multiply the pumping rate and making parallel reaction channels into a close loop for self-circulation.

4.2 Principle Illustration

O_2 gas usually as the anode of hydrogen-oxygen or other fuel cell source, is able to be generated, collected and stored in microfluidic gas generator. This device allows the reaction,

$$2H_2O_2 \xrightarrow{\text{Pt}} 2H_2O + O_2 \uparrow$$

happens, as soon as O_2 bubble transfered into PTFE (polytetrafluoroethylene) membrane then to gas vent. The mechanism of fluid flow inside the channel is due to the virtual check valve and hydrophilic treatment of the channel, which is illustrated in Figure 4.1 and 4.2 separately.

Figure 4.1 depicts the capillary force difference ΔP between the virtual check valve narrow channel side and reaction channel wide side. ΔP_{max} when gas bubble goes through the virtual check valve, is presented due to Young equation below:

$$\Delta P_{max} = 2\sigma(\frac{1}{h_i} + \frac{1}{w_i})cos\theta$$

σ is surface tension, θ is receding contact angle in liquid and solid interface, in this scenario, θ does not change at both side and h_i and w_i presents the channel height, and width. i=1,2 represents the narrow side channel and wide side channel. Because $h \leq h_2$, $w_1 = w_2$, θ receding contact angle is same at both side of channel. So $\Delta P_{max2} \ll \Delta P_{max1}$ that means the flow is moved directly from narrow side channel to wide side channel.

Figure 4.2 depicts the effect of hydrophilic and hydrophobic treatment on channel surface. In this scenario, h_i and w_i do not change, but compared in equation (4.2), the receding contact angle from liquid to gas interface, $\theta_t \leq \theta_f$, that means $cos\theta_f \leq \theta_t$,

and then $\Delta P_{maxf} \ll \Delta P_{maxt}$, flow easily goes through the hydrophilic part rather than the hydrophobic part of the channel.

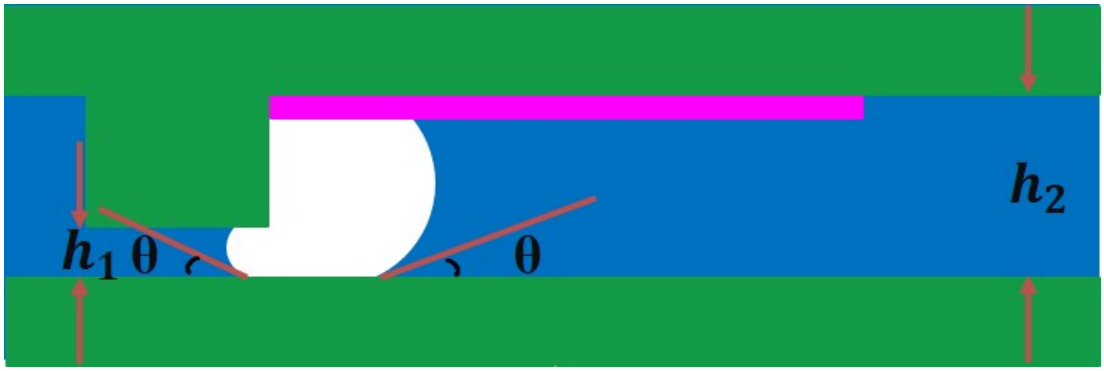

Fig. 4.1. Capillary force at the virtual check valve

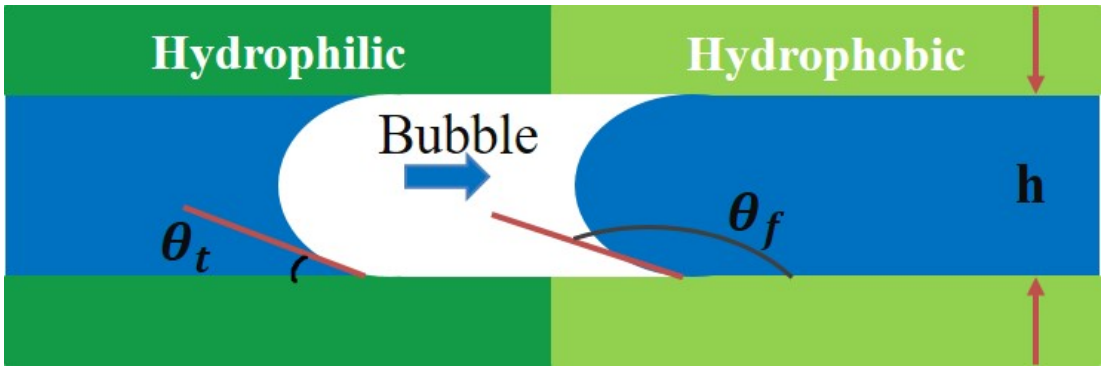

Fig. 4.2. Hydrophilic vs. hydrophobic effect

4.3 Results and Discussion

Advanced fabrication method

Details about the advanced fabrication method of microfluidic gas generator is given in Yuanzhi Cao's thesis. To begin with fabrication of either single or triple reaction channel device should follow the instruction of design, fabrication, and post

processing. But in this section the fundamental procedures only to be mentioned for triple reaction channel design as accompanying below:

1. Device design and design sketch

   To fabricate or first step of production design, comes up with the stereotype function analysis, or function design. What form always follows what function. Our requirements for that microfluidic gas generator is to make the solution flow driven by capillary force difference at the virtual check valve of generating gas bubble. So virtual check valve and reaction channel should be connected through inlet to outlet, and gas collector is necessary as well to directly hooked up with them.

   To clarify the function design, a design sketch is needed to record any enlightening idea.

2. Model building

   After have the sketch, the design in embryo should be put in either 2D or 3D modeling to obtain a visualized design using any CAD (computer aided design) software. To fulfill our requirements, the model consists of at least 11 layers. The cross sectional view is given as an example of the single channel gas generator shown in Figure 4.3. The pink highlight part is where Pt catalyst attached.

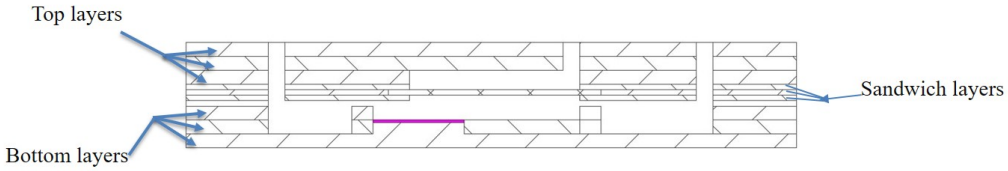

Fig. 4.3. AutoCAD cross-section view of the device.

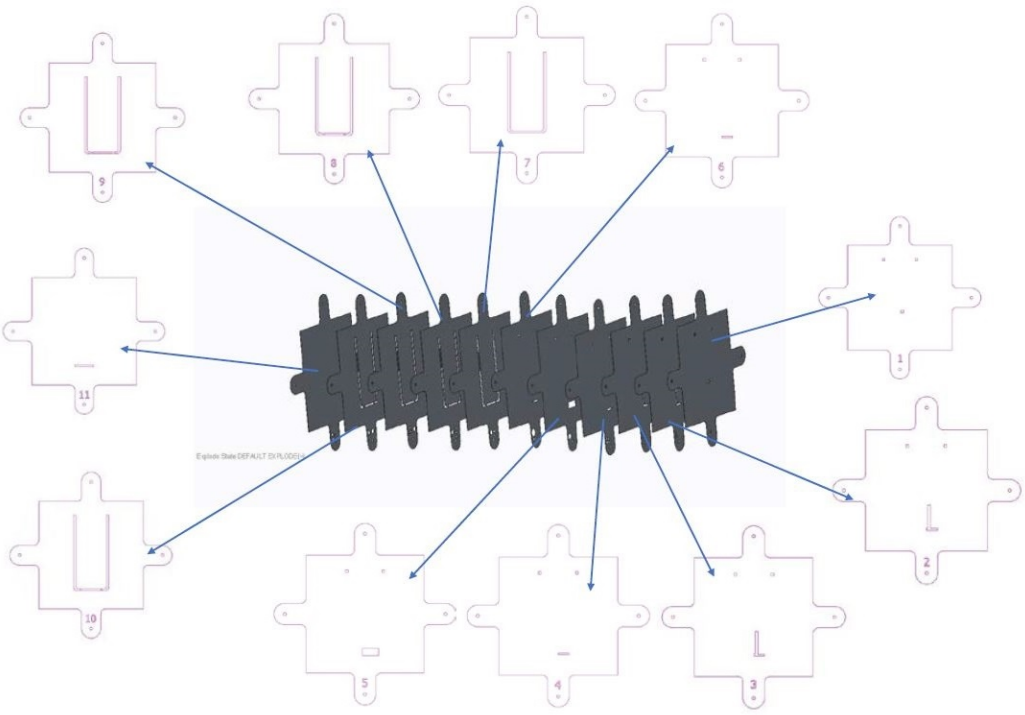

Fig. 4.4. Explosive view of each layer.

3. Export 2D drawings for each subassembly

   As for our microfluidic gas generator, the assembly includes sequentially stacking and integrating layers, so the subassembly is each layer. The manufacturing approach of each subassembly is subtractive processing. So it is in need to export the 2D drawings of each layer for the digital cutter (FC2250-60 VC, Graphtec, Santa Ana, CA) in SL067 to cut. [46] The explosive view combined with top view of each layer is shown in Figure 4.4 for patterning.

4. Material preparation

   Step 1: PS films preparation Before get patterned each layer, two kind thickness of PS films are needed for digital cutting:

   - A piece of enough space of 125 μm PS film.
   - A piece of enough space of 50 μm PS film.

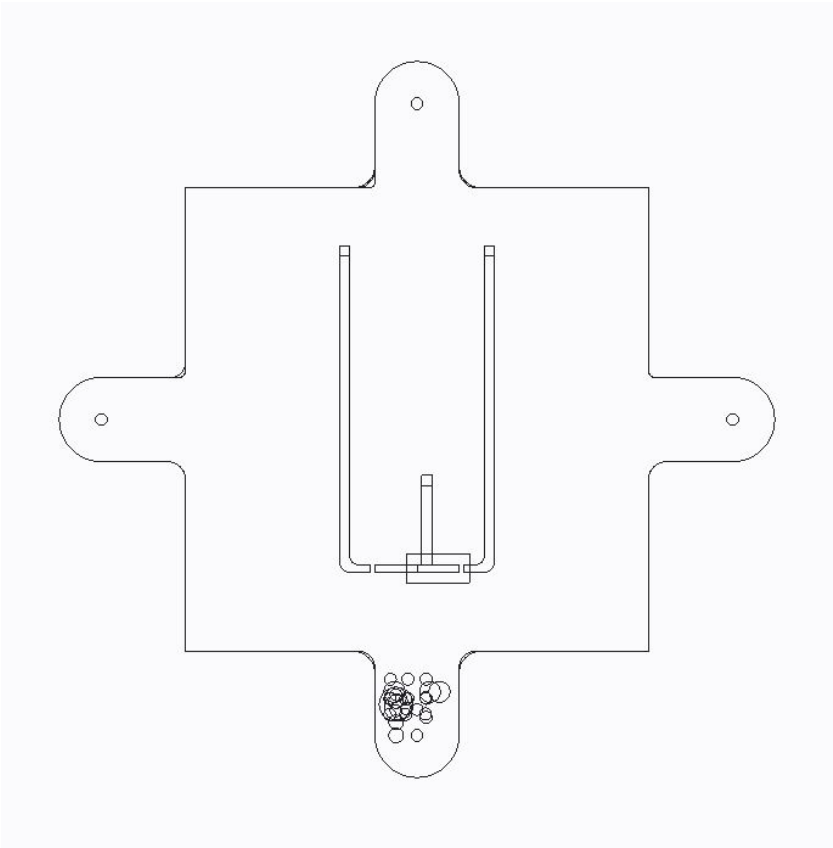

Fig. 4.5. Top view of the microfluidic gas generator by draft.

Then need 0.2 μm pore size vent PTFE membrane and 1 piece of enough space of catalyst (Pt has been electroplated on a gold foil by a substitution reaction, attached by the double sided tape), and also tape, scissor, as well as tweezer.

To protect the fragile PS films either thickness of 125 μm or 50 μm, is to adhere the thin Poly Carbonate film for both side of layer.

Step 2: Pt catalyst electroplating

The electroplating time and current density were calculated. The source used for that process is similar system with Arbin power machine.

5. PS film pattern cutting

   To use the digital cutting machine, training on operation and safety is needed. The key point of cutting largely determines the performance of pattern by the extrusion tip of the cutter blade. Mark the proper position of extrusion for either 125 μm layer and 50 μm layer. Another crucial information is that how to cut the PTFE membrane and Pt catalyst on tape properly.

   Step 3: PS film cutting post-processing

   Tare care of tearing apart the patterned layers and collect them in a clean Petri dish with cover.

6. Thermo-press bonding

   After material preparation, the thermo-press bonding process classified as three main procedure:

   (a) Combine 10^{th} layer and two of 11^{th} layer aligning by 4 pins in each side with proper Pt catalyst adhered. The bonding is sandwiched inside two glass plate between the two hydraulic pressure plate (20 mins, the hydraulic pressure between the top and bottom plate is 4000 psi, 200 °F temperature).

   (b) Add 8^{th}, 9^{th}layer on top of the the part at (a) (20 mins, the hydraulic pressure between the top and bottom plate is 4000 psi, 200 °F temperature).

   (c) Before each bonding process, each layer should be washed by ethanol solution, DI (deionized) watter and dry up by clean air gun.

   (d) Combine 4^{th}, 5^{th}, 6^{th} layers together with a membrane embedded in the 5^{th} layer (15 mins, the hydraulic pressure between the top and bottom plate is 4000 psi, 200 °F temperature).

   (e) Combine 2^{nd}, and 3^{rd} layer together. (10 mins, the hydraulic pressure between the top and bottom plate is 4000 psi, 200 °F temperature).

(f) Add two of 1^{st} on the top of 2^{nd} layer. (20 mins, the hydraulic pressure between the top and bottom plate is 4000 *psi*, 200 °F temperature).

(g) Finally with sequence combine all the part together. (60 mins, the hydraulic pressure between the top and bottom plate is 4000 *psi*, 200 °F temperature, Kill the heat at 30 mins and after 30 mins shut down the power of the bonding machine).

Figure 4.5 and 4.6 are 2D AutoCad assembly and real work device with inject connector after themo-fabrication.

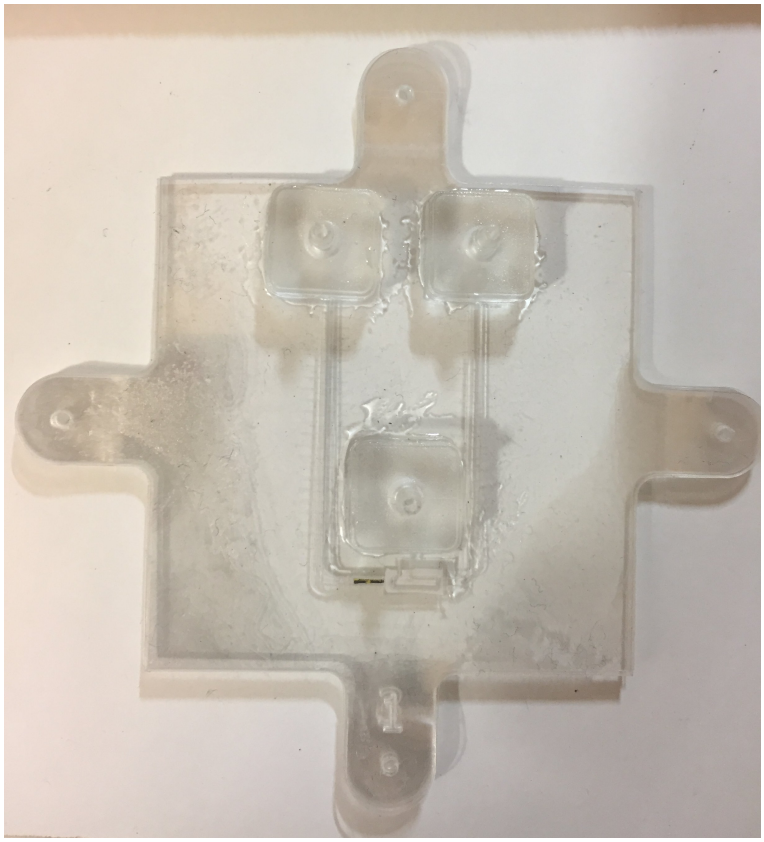

Fig. 4.6. Top view of the real worked microfluidic gas generator.

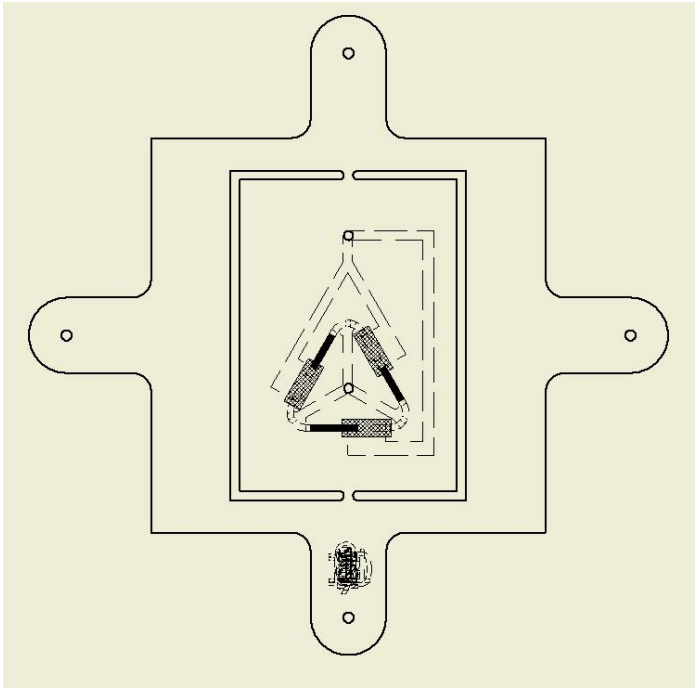

(a) Top view of assembled triple reaction channel design

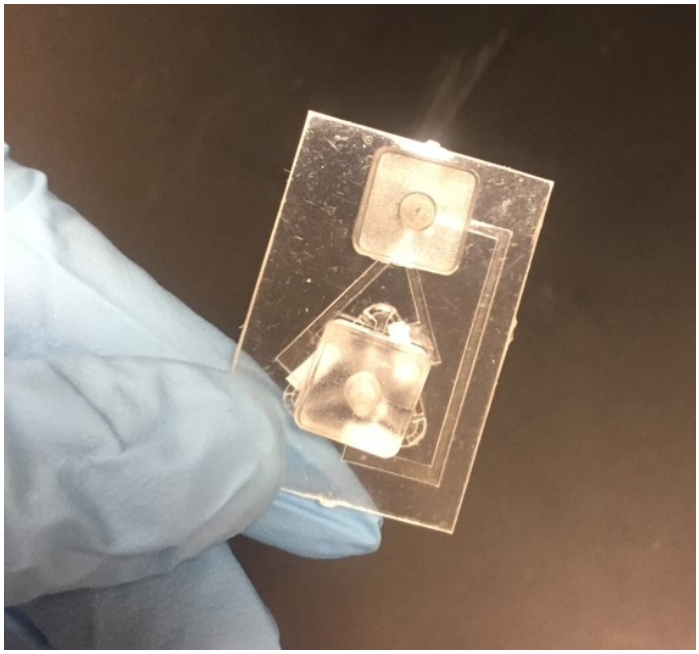

(b) Triple reaction channel actual device

Fig. 4.7. Triple reaction channel design

Device Testing

After fabrication and connectors adhered on the surface of inlet, outlet and gas vent, using Epoxy glue in 24 hours fix up see Figure 4.6.

The syringe pump was applied to pump 30% H_2O_2 solution from inlet with a $0.3 \sim 0.4$ psi back pressure on the gas vent to see how reaction channel works with reactant solution. Also using the OMEGA gas flow meter (OMEGA Engineering, INC., Norwalk, CT 06854) was used to measure device generating O_2 goes into the gas vent. Connect the gas meter with Labjack measurement automation device (LabJack Corporation, CO 80227, USA) to a computer, recording the flow rate data by the frequency of 1 data/sec. The pumping rate of the syringe is 0.2 $\mu L/s$. [5]

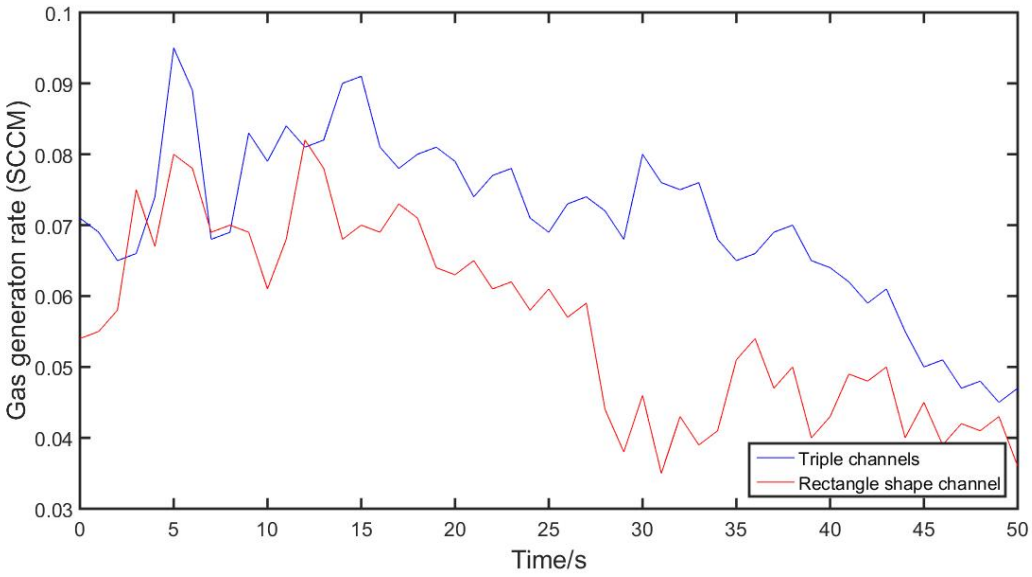

Fig. 4.8. Gas generation rate in 50 s.The blue solid line presents the gas generator of triple parallel reaction channels. The red solid line represents the gas generator has single one reaction channel. Both generator has the same rectangle reaction channel shape.

A compared profile was shown in Figure 4.8 for O_2 generation rate measured on single reaction channel device and triple parallel channel device. The first similarity of

the red and blue line is the constant drop of gas generation rate, due to the resistance pressure between inlet and outlet channel for self-circulation. Then at the beginning of reaction, from 0 s to 15 s, more O_2 gas was produced and exhausted from reaction channel to gas vent contrast to when finishing collecting data at 50 s. The highest gas generation rate for triple parallel channel device is 0.095 $SCCM$ at 5 s, while for single channel device is 0.083 $SCCM$ at 13 s. Because of the data collection method and the dramatical reaction, the gas generation rate is not enabled to be steady at any two continuous second and always varies with time evolution. Clear to see that after approximate 25 s, the O_2 generation flop down largely, resulting in the consumption of H_2O_2 and Pt catalyst layer. Another reason is supposed to be the generated water volume take large space in the channel and mitigate the reactant solution rate. Make the reaction inactive. Generally speaking, the reaction channel with a triple parallel rectangle design has a better gas generation characteristic than the single one and in the same time period, would provide and vent more O_2 gas.

4.4 Conclusion

In this chapter illustrates a renewal device that optimized reaction area with triple rectangle parallel channel design. The fabrication method is summarized and reorganized from previous work to avoid delamination and enhance gas generation rate. From the above gas generation test results, compared with single channel device, tripe channel device has a much better and stable gas generation performance. Based on these dimensional values for a single reaction channel, we can design and fabricate microfluidic devices with multiple serial and channels. The O_2 gas generation rate from a triple channel design is higher than single channel device during reaction happens, especially the first 10 s. The more stable gas generation rate was obtained from the parallel design device. Our advanced themo-press bonding fabrication method has obviously advantages and features to process PS film-based microfluidic gas generator.

5. SUMMARY AND RECOMMENDATIONS

5.1 Summary

This thesis presents a series of studies on experimental and numerical microbubble coalescence dynamics through image processing and an advanced microfluilic gas generator.

In this thesis, the analysis of neck growth and surface wave propagation in the early stage of coalescence of different size ratio microbubbles captured on solid substrate were investigated experimentally and numerically. A special PS film-based microfluidic device was designed and fabricated to generate microbubbles and coalescence events. To visualize the individual coalescence event, synchrotron X-ray facility was applied from cross-section to gain a better understanding of the event. To procure much data, both 3D and 2D ANSYS FLUENT simulation was employed. The image study show that the neck growth dynamics of two microbubbles captive on a solid surface shows a half power-law with inertial-capillary time scale and controlled by the smaller parent microbubble, which is universal with size inequality and contact angle difference. The surface wave propagation on the larger parent microbubble follows a universal linear law with inertial-capillary time scale as well as no contact angle difference effect.

Meanwhile, aided by the high speed X-ray facility, coalescence preference study on unequal-sized microbubbles captive on solid substrate was presented. A power law indicates the relation between size inequality and preferential distance after merging.Our results and analysis show that after merging the horizontal preference position of the new sphere can be placed less closer to the larger parent bubble. The power-law of relative position d_L/d_S and bubble size inequality r_L/r_S is quite different from that surface energy theory given for free bubbles that are not confined in channel

and attached on a solid interface. This result would be important to understand the coalescence dynamics under different situations and further study on surface energy released between solid interface and liquid interface. The potential explanation to reconcile is that wall shear stress takes significant effect on hindering new merged bubble towards the larger bubble. Additionally, the partial study on displacement of contacting points has representative the microbubble pair shifting tendency on the ground.

For experimental microbubble coalescence study, the integrated microfluidic gas generator with proper performance takes advantages. Triple parallel reaction channel device was represented, tested and compared with one with single reaction channel. The O_2 gas generation rate from a triple channel design is higher than single channel device during reaction happens, especially the first 10 s. The more stable gas generation rate was obtained from the parallel design device. Our advanced themo-press bonding fabrication method has obviously advantages and features to process PS film-based microfluidic gas generator. Our advanced themo-press bonding fabrication method has obviously advantages and features to process PS film-based microfluidic gas generator.

5.2 Recommendations

Based on what we have achieved on the study of microbubble coalescence dynamics and microfluidic gas generation, the followings are given as a recommendation for future work.

1. Make comparison study on Centroid oscillation of microbubbles during merging experimentally and numerically, to process the image study. To accomplish it, an advance post-processing software AVIZO can be used.

2. Measure and collect enough data on preference analysis from ANSYS FLUENT 3D simulation to confirm our results from experiment.

3. The fabrication and test on serial reaction channel with rectangle shape can improve our knowledge on integrated microfluidic gas generator study. The self-circulation design should be discussed and modified.

4. The initial distance between two separate microbubbles attached on the solid substrate should provide information on coalescence taking place.

These future works would help us gain a deeper knowledge of micro-scale bubble coalescence dynamics and wide-range applications of device.

REFERENCES

REFERENCES

[1] R. Chen, H. W. Yu, L. Zhu, R. M. Patil, and T. Lee, "Spatial and temporal scaling of unequal microbubble coalescence," *AIChE Journal*, vol. 63, no. 4, pp. 1441–1450, 2017.

[2] R. L. Stover, C. W. Tobias, and M. M. Denn, "Bubble coalescence dynamics," *AIChE journal*, vol. 43, no. 10, pp. 2385–2392, 1997.

[3] J. Goldsmith, A. G. Wong-Foy, M. J. Cafarella, and D. J. Siegel, "Theoretical limits of hydrogen storage in metal–organic frameworks: Opportunities and trade-offs," *Chemistry of Materials*, vol. 25, no. 16, pp. 3373–3382, 2013.

[4] C. Knight, K. Cavanagh, C. Munnings, T. Moore, K. Y. Cheng, and A. H. Kaksonen, "Application of microbial fuel cells to power sensor networks for ecological monitoring," *Wireless Sensor Networks and Ecological Monitoring*, vol. 3, pp. 151–78, 2013.

[5] Y. Cao, J. Bontrager-Singer, and L. Zhu, "A 3d microfluidic device fabrication method using thermopress bonding with multiple layers of polystyrene film," *Journal of Micromechanics and Microengineering*, vol. 25, no. 6, p. 065005, 2015.

[6] E. Selli, G. L. Chiarello, E. Quartarone, P. Mustarelli, I. Rossetti, and L. Forni, "A photocatalytic water splitting device for separate hydrogen and oxygen evolution," *Chemical communications*, no. 47, pp. 5022–5024, 2007.

[7] M. G. Walter, E. L. Warren, J. R. McKone, S. W. Boettcher, Q. Mi, E. A. Santori, and N. S. Lewis, "Solar water splitting cells," *Chemical reviews*, vol. 110, no. 11, pp. 6446–6473, 2010.

[8] C. L. Muhich, B. D. Ehrhart, I. Al-Shankiti, B. J. Ward, C. B. Musgrave, and A. W. Weimer, "A review and perspective of efficient hydrogen generation via solar thermal water splitting," *Wiley Interdisciplinary Reviews: Energy and Environment*, vol. 5, no. 3, pp. 261–287, 2016.

[9] J. Ditzig, H. Liu, and B. E. Logan, "Production of hydrogen from domestic wastewater using a bioelectrochemically assisted microbial reactor (beamr)," *International Journal of Hydrogen Energy*, vol. 32, no. 13, pp. 2296–2304, 2007.

[10] B. E. Logan, D. Call, S. Cheng, H. V. Hamelers, T. H. Sleutels, A. W. Jeremiasse, and R. A. Rozendal, "Microbial electrolysis cells for high yield hydrogen gas production from organic matter," *Environmental science & technology*, vol. 42, no. 23, pp. 8630–8640, 2008.

[11] B. E. Logan, "Scaling up microbial fuel cells and other bioelectrochemical systems," *Applied microbiology and biotechnology*, vol. 85, no. 6, pp. 1665–1671, 2010.

[12] P. D. Vaidya and E. Y. Kenig, "Gas–liquid reaction kinetics: a review of determination methods," *Chemical Engineering Communications*, vol. 194, no. 12, pp. 1543–1565, 2007.

[13] R. Kaur, M. Ramakrishna, and K. Nigam, "Role of dispersed phase in gas-liquid reactions: A review," *Reviews in Chemical Engineering*, vol. 23, no. 3-4, pp. 247–300, 2007.

[14] R. Dittmeyer, K. Svajda, and M. Reif, "A review of catalytic membrane layers for gas/liquid reactions," *Topics in catalysis*, vol. 29, no. 1, pp. 3–27, 2004.

[15] J. D. Paulsen, R. Carmigniani, A. Kannan, J. C. Burton, and S. R. Nagel, "Coalescence of bubbles and drops in an outer fluid," *arXiv preprint arXiv:1407.6657*, 2014.

[16] E. Egan and C. Tobias, "Measurement of interfacial re-equilibration during hydrogen bubble coalescence," *Journal of the Electrochemical Society*, vol. 141, no. 5, pp. 1118–1126, 1994.

[17] D. Li, "Coalescence between small bubbles: effects of surface tension gradient and surface viscosities," *Journal of colloid and interface science*, vol. 181, no. 1, pp. 34–44, 1996.

[18] V. V. Yaminsky, S. Ohnishi, E. A. Vogler, and R. G. Horn, "Stability of aqueous films between bubbles. part 1. the effect of speed on bubble coalescence in purified water and simple electrolyte solutions," *Langmuir*, vol. 26, no. 11, pp. 8061–8074, 2010.

[19] R. G. Rice, "Analytical solutions for film thinning dynamics in bubble coalescence," *AIChE journal*, vol. 52, no. 4, pp. 1621–1622, 2006.

[20] C. R. Anthony, P. M. Kamat, S. S. Thete, J. P. Munro, J. R. Lister, M. T. Harris, and O. A. Basaran, "Scaling laws and dynamics of bubble coalescence," *Physical Review Fluids*, vol. 2, no. 8, p. 083601, 2017.

[21] J. Eggers, J. R. Lister, and H. A. Stone, "Coalescence of liquid drops," *Journal of Fluid Mechanics*, vol. 401, pp. 293–310, 1999.

[22] Y. Kim, S. J. Lim, B. Gim, and B. M. Weon, "Coalescence preference in densely packed microbubbles," *Scientific reports*, vol. 5, p. 7739, 2015.

[23] B. M. Weon and J. H. Je, "Coalescence preference depends on size inequality," *Physical review letters*, vol. 108, no. 22, p. 224501, 2012.

[24] E. Stenmark, "On multiphase flow models in ansys cfd software," *Department of Applied Mechanics Division of Fluid Dynamics. Chalmers university of technology. Göteborg, Sweden*, vol. 75, 2013.

[25] A. Kazemzadeh, P. Ganesan, F. Ibrahim, S. He, and M. J. Madou, "The effect of contact angles and capillary dimensions on the burst frequency of super hydrophilic and hydrophilic centrifugal microfluidic platforms, a cfd study," *PloS one*, vol. 8, no. 9, p. e73002, 2013.

[26] J. E. Sprittles and Y. D. Shikhmurzaev, "A parametric study of the coalescence of liquid drops in a viscous gas," *Journal of Fluid Mechanics*, vol. 753, pp. 279–306, 2014.

[27] H. Zheng, C. Shu, and Y.-T. Chew, "A lattice boltzmann model for multiphase flows with large density ratio," *Journal of Computational Physics*, vol. 218, no. 1, pp. 353–371, 2006.

[28] Y. Egorov, F. Menter, R. Lechner, and D. Cokljat, "The scale-adaptive simulation method for unsteady turbulent flow predictions. part 2: Application to complex flows," *Flow, Turbulence and Combustion*, vol. 85, no. 1, pp. 139–165, 2010.

[29] D. Chandler, "Interfaces and the driving force of hydrophobic assembly," *Nature*, vol. 437, no. 7059, pp. 640–647, 2005.

[30] J. W. Kim and W. K. Lee, "Coalescence behavior of two bubbles in stagnant liquids," *Journal of Chemical Engineering of Japan*, vol. 20, no. 5, pp. 448–453, 1987.

[31] A. Slone, K. Pericleous, C. Bailey, and M. Cross, "Dynamic fluid–structure interaction using finite volume unstructured mesh procedures," *Computers & structures*, vol. 80, no. 5, pp. 371–390, 2002.

[32] J. Brackbill, D. B. Kothe, and C. Zemach, "A continuum method for modeling surface tension," *Journal of computational physics*, vol. 100, no. 2, pp. 335–354, 1992.

[33] T. Fu, Y. Ma, and H. Z. Li, "Bubble coalescence in non-newtonian fluids in a microfluidic expansion device," *Chemical Engineering and Processing: Process Intensification*, vol. 97, pp. 38–44, 2015.

[34] P. M. Somwanshi, K. Muralidhar, and S. Khandekar, "Wall shear rates generated during coalescence of pendant and sessile drops," *Fluid Mechanics and Fluid Power–Contemporary Research*, pp. 33–42, 2017.

[35] K. Tse, T. Martin, C. McFarlane, and A. Nienow, "Small bubble formation via a coalescence dependent break-up mechanism," *Chemical Engineering Science*, vol. 58, no. 2, pp. 275–286, 2003.

[36] T.-J. Lin and G.-M. Lin, "The mechanisms of bubble coalescence in a non-newtonian fluid," *The Canadian Journal of Chemical Engineering*, vol. 81, no. 3-4, pp. 476–482, 2003.

[37] C. Wang, W. Hung, S. Fu, W. Huang, and C. Law, "On the burning and microexplosion of collision-generated two-component droplets: miscible fuels," *Combustion and flame*, vol. 134, no. 3, pp. 289–300, 2003.

[38] K. E. Kenyon, "Capillary waves understood by an elementary method," *Journal of Oceanography*, vol. 54, no. 4, pp. 343–346, 1998.

[39] F. Behroozi and A. Perkins, "Direct measurement of the dispersion relation of capillary waves by laser interferometry," *American journal of physics*, vol. 74, no. 11, pp. 957–961, 2006.

[40] F. Zhang and S. Thoroddsen, "Satellite generation during bubble coalescence," *Physics of Fluids*, vol. 20, no. 2, p. 022104, 2008.

[41] P. Mitchell, "Microfluidics–downsizing large-scale biology," *Nature biotechnology*, vol. 19, no. 8, p. 717, 2001.

[42] G. M. Whitesides, "The origins and the future of microfluidics," *Nature*, vol. 442, no. 7101, pp. 368–373, 2006.

[43] M. A. Burns, "Everyone's a (future) chemist," *Science*, vol. 296, no. 5574, pp. 1818–1819, 2002.

[44] D. R. Meldrum and M. R. Holl, "Microscale bioanalytical systems," *Science*, vol. 297, no. 5584, pp. 1197–1198, 2002.

[45] S. K. Sia and G. M. Whitesides, "Microfluidic devices fabricated in poly (dimethylsiloxane) for biological studies," *Electrophoresis*, vol. 24, no. 21, pp. 3563–3576, 2003.

[46] Y. Cao, "The development of polystyrene based microfluidic gas generation system," *Purdue University*, pp. 20–40, 2015.